

Assaying Macrophage Chemotaxis Using Fluid-Walled Microfluidics

Cyril Deroy, Agata N. Rumianek, James H. R. Wheeler, Federico Nebuloni, Peter R. Cook, David R. Greaves,* and Edmond J. Walsh*

While many tools exist to study immune-cell chemotaxis *in vitro*, current methods often lack desirable features. Using fluid-walled microfluidics, circuits are built around primary murine macrophages deposited in pre-defined patterns on Petri dishes or microplates. Concentration gradients of complement component 5a (C5a) are established in flow-free or flowing environments, cell migration imaged, and cell directionality and velocity correlated to calculated local C5a concentrations. In flow-free circuits built around patterned macrophages, only cells nearest the C5a source migrate regardless of local attractant concentration. Conversely, in flowing circuits free from intercellular signaling and attractant degradation, only cells distant from the source migrate. In both systems, cells respond to lower C5a concentrations than previously reported (≈ 0.1 pM). Finally, macrophages follow instantly-shifted gradients better than slowly-shifting ones, suggesting that migration depends on both spatial and temporal responses to concentration.

Various chemotaxis assays have been used since the 1960s but all have significant limitations. Transwell assays are technically simple and widely-used; a porous insert containing cells is placed inside a well loaded with attractant, and (once a concentration gradient is established by diffusion) cells migrate through micrometer-sized pores into the well, and chemotaxis is quantified by removing the insert and counting cells in the well.^[5] The xCELLigence assay provided a major technical advance; impedance changes are measured in real-time as cells travel through pores in a modified Boyden chamber.^[6] Alternatives to the transwell assay were introduced to address some of its limitations, including tracking and monitoring single cells (as in Dunn chambers),^[7] and detecting cell reversibility or fugetaxis (as in under-agarose migration assays).^[8] More recently, microfluidic systems have been developed^[9] that enable control of stable gradients,^[10] distinction between different types of movement (e.g., chemotaxis, chemokinesis—non-directional cell migration, and fuge-taxis^[11]), tracking individual cells in real-time,^[12] and increased throughput^[13]—sometimes achieved with less reliance on specialized equipment.^[14] While microfluidic approaches show great promise, their uptake in biomedical research has been impeded by the technical complexity required to operate devices, long fabrication and prototyping times, the problematic biocompatibility of the plastic often used (i.e., polydimethylsiloxane,

rose migration assays).^[8] More recently, microfluidic systems have been developed^[9] that enable control of stable gradients,^[10] distinction between different types of movement (e.g., chemotaxis, chemokinesis—non-directional cell migration, and fuge-taxis^[11]), tracking individual cells in real-time,^[12] and increased throughput^[13]—sometimes achieved with less reliance on specialized equipment.^[14] While microfluidic approaches show great promise, their uptake in biomedical research has been impeded by the technical complexity required to operate devices, long fabrication and prototyping times, the problematic biocompatibility of the plastic often used (i.e., polydimethylsiloxane,

1. Introduction

Cells often experience environments containing heterogeneous chemical signals. These signals can induce directed cell migration (i.e., chemotaxis) and play crucial roles in regulating tissue homeostasis and inflammation.^[1,2] For example, chemotactic signals are essential for immunity, as they direct neutrophils and monocytes to inflammation sites. Macrophages also respond to chemoattractants to discover and repair tissue damage, destroy infections, and maintain homeostasis. However, chemotaxis also contributes to pathological processes such as atherosclerosis.^[3,4]


C. Deroy, F. Nebuloni, E. J. Walsh
Department of Engineering Science
Osney Thermo-Fluids Laboratory
University of Oxford
Oxford OX2 0ES, UK
E-mail: edmond.walsh@eng.ox.ac.uk

A. N. Rumianek, P. R. Cook, D. R. Greaves
Sir William Dunn School of Pathology
University of Oxford
Oxford OX1 3RE, UK
E-mail: david.greaves@path.ox.ac.uk

J. H. R. Wheeler
Department of Physics and Astronomy
University of Sheffield
Sheffield S3 7RH, UK

J. H. R. Wheeler
Department of Zoology
University of Oxford
Oxford OX1 3SZ, UK

J. H. R. Wheeler
Department of Biochemistry
University of Oxford
Oxford OX1 3QU, UK

 The ORCID identification number(s) for the author(s) of this article can be found under <https://doi.org/10.1002/admt.202200279>.

© 2022 The Authors. Advanced Materials Technologies published by Wiley-VCH GmbH. This is an open access article under the terms of the Creative Commons Attribution License, which permits use, distribution and reproduction in any medium, provided the original work is properly cited.

DOI: 10.1002/admt.202200279

PDMS), and failure rates associated with air bubbles disturbing flow patterns.^[15,16]

Here, we introduce a microfluidic platform that provides a suite of chemotaxis assays for studying migration of adherent cells. These methods are based on an open microfluidic approach involving a recently-developed fluid-shaping technology^[17,18] in which circuits are printed in seconds using standard media on polystyrene Petri dishes or microplates. To demonstrate proof-of-principle, we examine the well-documented chemotaxis of primary murine bone-marrow-derived macrophages (BMDMs) towards complement component 5a (C5a)—a small peptide released at sites of infection.^[19] Cells are deposited in a user-specified pattern on a dish or well, and the desired circuit is built around them. Chemotactic gradients are then established by diffusion (in either flow-free or flowing environments), and migrating cells imaged as they migrate up the gradient. Inspection of individual cell trajectories reveals hitherto unseen macrophage behaviors that depend on spatiotemporal responses to concentration and neighboring cells.

2. Results

2.1. Workflow and Operation

2.1.1. Printing Circuits Around Living Cells

Circuits are printed on standard 35 mm Petri dishes using a custom-built ‘printer’ as described previously.^[18] Briefly, the printer consists of a 3-axis traverse that holds a dispensing needle used to add/remove liquids. We first print BMDMs in any desired 2D pattern by simply infusing culture medium containing suspended cells through the dispensing needle and onto the surface of a dish (Figure 1A(i)). The dish is incubated (5 min) so cells attach, and the bottom of the dish is then gently and completely covered with medium; as macrophages are strongly adherent, they remain firmly attached to the dish where originally deposited (Figure 1A(ii)). Most medium is now removed to leave a thin layer, which is immediately covered with FC40—a bioinert and liquid fluorocarbon that prevents evaporation. After returning the dish to the printer in the original orientation, another dispensing needle jets a stream of FC40 through the thin layer of medium onto the bottom of the dish (Figure 1A(iii)); this jet pushes medium aside so FC40 locally contacts—and adheres to—the bottom of the dish. This process reshapes the interface between medium and fluorocarbon, to create what we refer to as a fluid wall. The traverse then moves the jetting needle above the dish along a path that will define the footprint of the fluid walls that are built around the living cells. Here, we build dumbbell-shaped (Figure 1A(iv)) or ‘m’-shaped (Figure 1A(v)) circuits in seconds to minutes that are respectively used either without (passive) or with (active) syringe-pump driven fluid flows.

2.1.2. Loading and Generating Stable Gradients in Passive Circuits

In passive circuits, reagents are pipetted directly through the fluid walls into the circuit (Figure 1B(i–ii))—either manually

or robotically on the printer—before gradients are established by diffusion. It is essential therefore that this pipetting does not induce flows that distort gradients. This is achieved as follows. Initially, pressures in the passive, dumbbell-shaped circuit—which consists of two fluid chambers separated by a single straight conduit—are at equilibrium. Then, medium (1 μ L) is added to the top chamber (represented by red dye in Figure 1B(i)) to increase its Laplace pressure (defined as $\Delta P = \frac{\gamma}{R}$, where γ = interfacial tension, R = radius of curvature, and $P_{\text{top}} = 20$ Pa); consequently, medium starts to flow towards the bottom chamber (Figure 1B(ii)). Next, a smaller volume of chemoattractant (0.5 μ L) is added to the bottom chamber (represented by blue dye in Figure 1B(ii); $P_{\text{bottom}} = 11$ Pa). This increases the Laplace pressure in that chamber but decreases the pressure gradient in the whole system ($\Delta P_{\text{circuit}} = 9$ Pa). Once 0.25 μ L medium enters the bottom chamber (shown as red dye entering the blue chamber in Figure 1B(iii)), the system reaches equilibrium. This procedure ensures that the pressure in the conduit is greater than P_{bottom} after adding the chemoattractant, so that no attractant can flow out of the bottom chamber into the conduit (Figure 1B(iv,v)). Instead, upon reaching equilibrium, attractant simply diffuses out of the bottom chamber to create a gradient from the bottom to the top of the conduit.

2.1.3. Determining Steady-State Times and Gradient Stability

The rate of change in concentration of a substance by diffusion is described by Fick’s second law as $\frac{\partial c}{\partial t} = D \frac{\partial^2 c}{\partial x^2}$

(c = concentration, t = time, x = distance, D = diffusion coefficient). During an initial transient phase, the concentration gradient in the conduit is defined using the 1D solution to the diffusion equation in a semi-infinite medium,

$c(x,t) = c_{\text{max}} \operatorname{erfc}\left(\frac{x}{2\sqrt{Dt}}\right)$ (c_{max} = concentration at the boundary).^[20] We arbitrarily say the system reaches equilibrium when the attractant concentration at the top of the conduit reaches 15% of the initial concentration in the bottom chamber, c_{max} . Then, the time required for the gradient to reach steady-

state, t_{SS} , is $\frac{x_{\text{conduit}}^2}{4D \times \operatorname{erfc}^{-1}(0.15)^2}$, where x_{conduit} = conduit length.

After reaching steady-state, the gradient in the conduit is linear and set to vary from 0 to 10 nM ($c_{\text{max}} = 10$ nM). As $t_{\text{SS}} \propto x^2$, doubling conduit length quadruples t_{SS} (e.g., for C5a in our system, if $x = 2$ mm, $t_{\text{SS}} \approx 1.5$ h; if $x = 4$ mm, $t_{\text{SS}} \approx 6$ h; Table S1, Supporting Information).

We next determine the rate of mass transfer through a conduit from Fick’s first law of diffusion $J = -D \frac{dc}{dx}$ ($J = \frac{\dot{m}}{A}$, \dot{m} = mass flow rate, A = area) to assess the duration of these stable gradients (and predict maximum experimental runtimes). Assuming the concentration gradient remains approximately constant until 5% of the analyte’s initial concentration c_{max} reaches the top chamber where it becomes evenly distributed ($c_{\text{end}} = 0.05c_{\text{max}}$), we define the maximum experimental

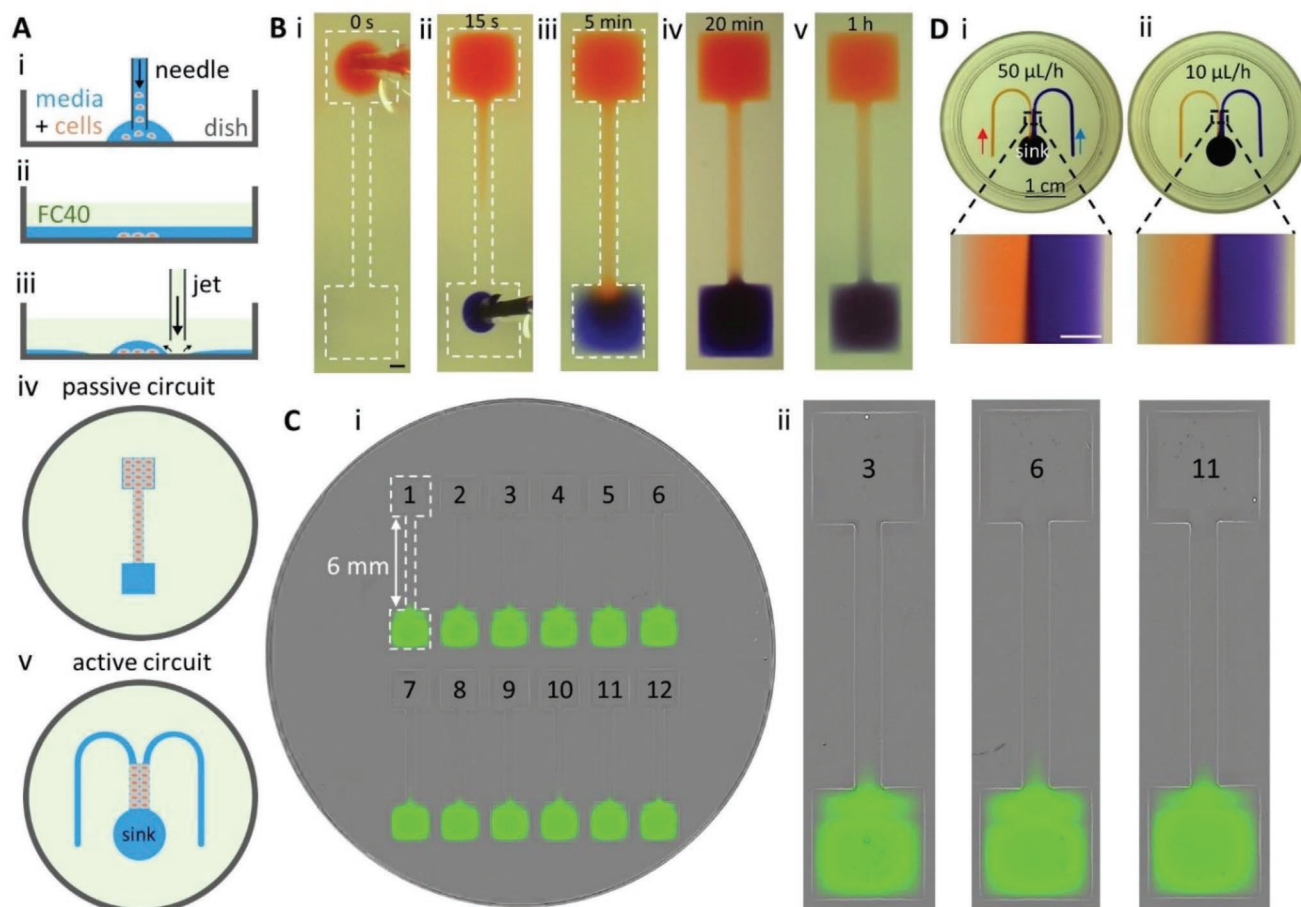


Figure 1. Printing and operating passive and active circuits. A) Printing passive and active circuits around patterned cells. i) A needle infuses medium + cells on a dish; moving the needle laterally deposits cells in the desired pattern. ii) Once cells attach, the bottom of the dish is covered with medium, most medium removed to leave $\approx 50 \mu\text{L}$ in a thin layer, and FC40 (2 mL) overlaid. iii) A needle loaded with FC40 is lowered into FC40 until just above the medium, and jets FC40 onto the dish to replace medium with FC40 that remains locally stuck to the dish. Moving the jet around cells now creates a continuous isolating FC40 wall and the desired circuit. iv) Flow-free (passive) dumbbell circuit. Cells are dispensed to form a rectangular drop, and a dumbbell-shaped wall is jetted around them. v) Active 'm'-shaped circuit. Cells are dispensed in a central rectangle and walls jetted around them to create the circuit. B) Establishing gradients in a passive dumbbell circuit. Red and blue dyes represent medium \pm C5a, respectively. Dashed lines: wall footprints. Scale bar = $500 \mu\text{m}$. i) Red dye ($1 \mu\text{L}$) is manually pipetted into the top chamber. ii) Resulting pressure differences induce advective flow down the conduit. A volume of blue dye too small to reverse this flow ($0.5 \mu\text{L}$) is pipetted into the bottom chamber. iii) After 5 min, red dye has entered the bottom chamber, the system equilibrates, and diffusion now establishes the gradient. iv) Blue dye starts to diffuse up the conduit. v) After 1 h, linear concentration gradients of each dye are established. C) Gradients in dumbbells remain undistorted as dishes are moved from printer to microscope. i) Image of a whole 35 mm dish containing 12 identical dumbbells formed by stitching together smaller images. Medium \pm fluorescein is loaded into upper and lower chambers as in (B) by a printer, the dish transferred to a microscope, images collected after 20 min, and stitched together. The fluorescein front diffuses up the conduit to reach essentially the same place in all 12 conduits. Incorrect stitching by the software yields apparently fluorescein-free lines at the top of lower chambers. ii) Close-ups of 3 circuits. D) Establishing gradients in an active 'm'-shaped circuit. i) Image of circuit as dyes are infused continuously (each at $25 \mu\text{L h}^{-1}$) through flanking arms to flow as laminar streams down the central conduit. Diffusion creates a gradient across the conduit. Inset: gradient width increases down the conduit (scale bar = $500 \mu\text{m}$). ii) As (i), but now dyes are each infused at $5 \mu\text{L h}^{-1}$. Inset: the gradient is shallower, as dyes have more time to diffuse (as flow is slower).

runtime as $t_{\text{end}} = 1.05 \frac{x m_{\text{C5a}}}{D A c_{\text{max}}}$ (A = conduit cross-sectional area, m_{C5a} = mass of C5a). The cross-sectional area of a conduit is expressed as $A = \frac{a^2}{2 \sin^2 \theta} \left(\frac{\theta \pi}{90} - \sin 2\theta \right)$, where a = conduit half-width and θ = contact angle. In this study, conduits have fixed widths so $t_{\text{end}} \propto x$, thus t_{end} varies proportionally with conduit length (e.g., for $x = 2 \text{ mm}$, $t_{\text{end}} \approx 15 \text{ h}$; for $x = 4 \text{ mm}$, $t_{\text{end}} \approx 30 \text{ h}$; Figure S1 and Table S1, Supporting Information).

2.1.4. Moving Dishes Containing Passive Circuits Does Not Impair Gradient Formation

As passive circuits are prepared on the printer and moved to a microscope for imaging, movement-induced advective flows could perturb gradients; therefore, we monitor gradient uniformity as follows. Twelve circuits are printed and loaded with fluorescein on the printer (in a biosafety cabinet to ensure sterility), moved to an imaging system (an IncuCyte ZOOM in an

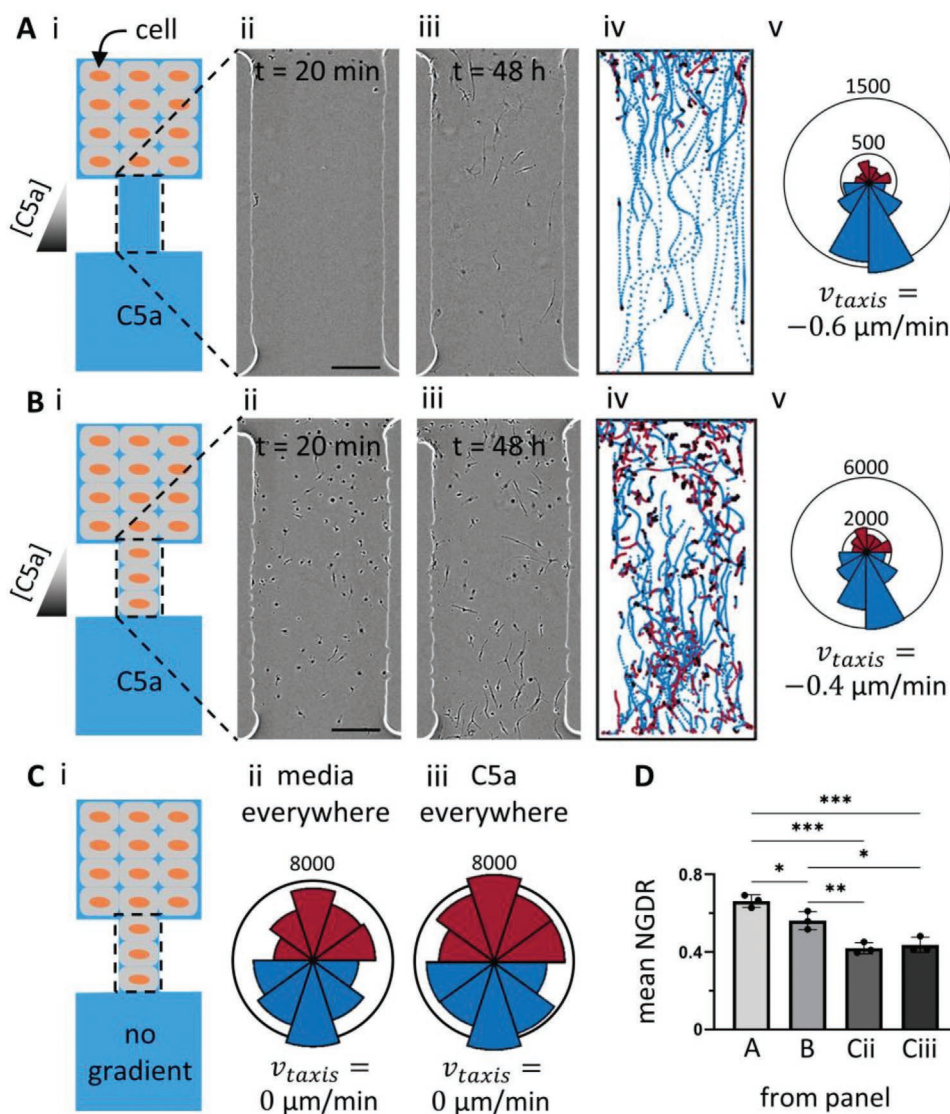


Figure 2. Tracking chemotactic bias in dumbbells jetted around BMDMs. C5a (10 nM) is generally added to the bottom chamber, time-lapse movies (phase contrast) of the conduit made over 48 h, trajectories of individual cells extracted, and rose plots generated (3 biological repeats for each condition). A) Migration of cells initially presents only in the top chamber. (i) Cartoon showing starting positions of cells (grey with orange nuclei). ii,iii) Images of conduit. Cells migrate into an empty conduit; many are elongated with characteristic pseudopodia. Scale bar = 250 μm . iv) Cell trajectories. Downward tracks towards C5a (blue) outnumber upward ones (red). Black tracks: stationary cells. v) Rose plot with the circles indicating number of trajectory points falling into each bin and measurements of v_{taxis} confirming this bias. B) Migration of cells initially present in top chamber and conduit. i) Cartoon showing starting positions of cells. ii,iii) Images of conduit; many cells become elongated. Scale bar = 250 μm . iv) Trajectories are again biased towards C5a. v) Rose plot with the circles indicating number of trajectory points falling into each bin and measurements of v_{taxis} confirming this bias. C) Controls. i) Cells initially present in the top chamber + conduit and rose plots with ii) medium alone or iii) with C5a in both chambers show lack of bias. D) Mean NGDR (\pm SD, 3 biological replicates) for C5a gradients from conditions in panels A, B, C(ii), and C(iii); one-way ANOVA statistical significance * $P < 0.033$, ** $P < 0.0021$, *** $P < 0.0002$.

incubator), and scanned using fluorescence; fluorescent fronts in all conduits are located in essentially the same places, consistent with little advective perturbation (Figure 1C).

2.1.5. Setting Up Gradients in Active Circuits

The passive circuits described previously have the advantage of being simple to set up and do not require external pumps;

however, their gradients change over time as diffusion drives the system to equilibrium. In contrast, gradients generated by diffusion between two laminar streams (one containing attractant) flowing continuously through one conduit remain stable and unchanging for as long as flow continues. Stable gradients in 'm'-shaped circuits—consisting of two circuit arms leading into a single central conduit—are thus established. Briefly, two needles are inserted separately into left and right arms of the circuit; needles are filled with medium \pm attractant

and are connected via polytetrafluoroethylene (PTFE) tubing to two syringes on one syringe pump. The syringes now start infusing at a constant flow rate, so medium (red dye added in Figure 1D(i)) and medium + attractant (represented by blue dye in Figure 1D(ii)) meet as laminar streams in the central conduit. Diffusion then creates a stable concentration gradient across the width of the conduit. The steepness of this gradient is controlled by varying the overall flow rate in the conduit (lower rates yield shallower gradients, Figure 1D(ii)). A third needle connected to another syringe on a separate pump is inserted into a sink at the end of the central conduit and withdraws fluid at an equivalent flow rate.

2.2. Chemotaxis of BMDMs in Passive (Flow-Free) Circuits

2.2.1. Exposing BMDMs to Gradients of C5a

We demonstrate the approach by monitoring chemotaxis of BMDMs in response to a gradient of C5a that varies from 0 to 10 nM—the concentration eliciting the strongest chemotactic response in transwell dose-response experiments (Figure S2, Supporting Information). Initially, all cells are in the top chamber of a dumbbell-shaped circuit (Figure 2A(i)), C5a (10 nM) is pipetted into the bottom chamber, and a time-lapse movie is made of the conduit over the next 48 h (Movie S1, Supporting Information; 1 frame every 20 min). Almost no cells are seen in the first movie frame (Figure 2A(ii)). As the gradient becomes established ($t_{SS} = 0.9$ h), cells enter the conduit and by the last frame some even reach the bottom chamber (Figure 2A(iii)). Tracks of individual cell trajectories are now derived by analyzing successive images in the movie (Experimental Section); these tracks show a biased movement of cells towards C5a (Figure 2A(iv); blue tracks indicate movement towards C5a, red ones away from it, and black dots show static cells). Trajectories are also binned according to angle and displayed as rose plots (Figure 2A(v); blue segments indicate tracks moving towards C5a, and red ones away from it, with segment length reflecting the number of trajectory points per bin). We next build circuits around cells initially located in the conduit and examine the response of these cells to the same gradient (Figure 2B; Movie S2, Supporting Information). Many cells are visible in the first frame (Figure 2B(ii)), and only some trajectories are biased towards C5a (Figure 2B(iv)); in other words, only some cells chemotax, and rose plots confirm this (Figure 2B(v)).

2.2.2. Distinguishing Between Chemotaxis and Chemokinesis

In the absence of a gradient, BMDMs typically move randomly. Whilst rose plots clearly indicate that some cells exhibit directed movement in a C5a gradient (and so chemotaxis), rose plots from controls performed in circuits without C5a in either chamber (Movie S3, Supporting Information), or with the attractant initially in both chambers (Movie S4, Supporting Information), show no bias (Figure 2C(ii,iii)). We also quantify cells' average drift velocity in the direction of the attractant (v_{taxis} , average y-velocity) and net-to-gross displacement ratio

(NGDR) for each condition. v_{taxis} is calculated by averaging the y-velocities of each trajectory (positive velocities towards the top chamber, negative velocities towards the bottom chamber). Thus, in a gradient, negative values of v_{taxis} indicate biased movement towards C5a (Figure 2A(v),B(v)). In controls, $v_{\text{taxis}} = 0 \mu\text{m min}^{-1}$, confirming the absence of chemotactic bias (Figure 2C(ii,iii)). The NGDR is defined as the straight-line distance between start and end points of a trajectory divided by the total distance traveled along the path of the trajectory (see for instance,^[21]). Therefore, an NGDR of 1 indicates a cell travels in a straight line from start to finish irrespective of whether it is towards or away from attractant, while progressively lower values point to decreased directedness (Figure 2D). All these results confirm previous ones showing that C5a is a chemoattractant for BMDMs.^[19]

2.3. Assessing Population Dynamics in BMDM Chemotaxis Assays

2.3.1. Patterning Cells in Conduits Reveals Unique Population Dynamics

Thus far, we have imaged short conduits (length 1.5 mm) initially containing no cells, or those where cells are uniformly distributed everywhere. We now compare responses of cells distributed in 4 different patterns in longer 6 mm conduits (chosen to improve resolution, but note that now $t_{SS} = 13.6$ h). Initially, cells occupy either the whole conduit (Figure 3A, purple), or just the top (Figure 3B, green), middle (Figure 3C, red), or bottom third (Figure 3D, blue). Since all 4 conduits have the same dimensions and as bottom chambers are filled with the same C5a concentration, diffusion will establish identical gradients in all conduits that develop similarly over time. Remarkably, trajectories of cells at equivalent points along the y axis in the 4 conduits often differ. Thus, consider the conduit initially filled uniformly with cells: only cells in the bottom third yield long blue trajectories and a biased rose plot, whilst those above them do not (Figure 3A). This might be expected: responders lie close to the highest attractant concentration, and non-responders, far from it. Now consider the other three panels (Figure 3B–D). The front closest to C5a is always rich in responders, but this is found at different distances from the lower chamber. In other words, migratory responses of macrophages seem to depend more on the position of the cells at the front of the population, and not on the absolute C5a concentration expected at that point in the conduit. This result highlights one advantage of the approach: printing circuits around cells in precise user-defined patterns enables identification of new behaviors.

2.3.2. Determining the Lowest C5a Concentrations Eliciting Chemotaxis

We next determine the lowest C5a concentration eliciting chemotaxis (c_{min}) in each of the four circuits described in Figure 3. Macrophages move by extending pseudopodia that pull the cell over the substrate, and pseudopodia extending towards an

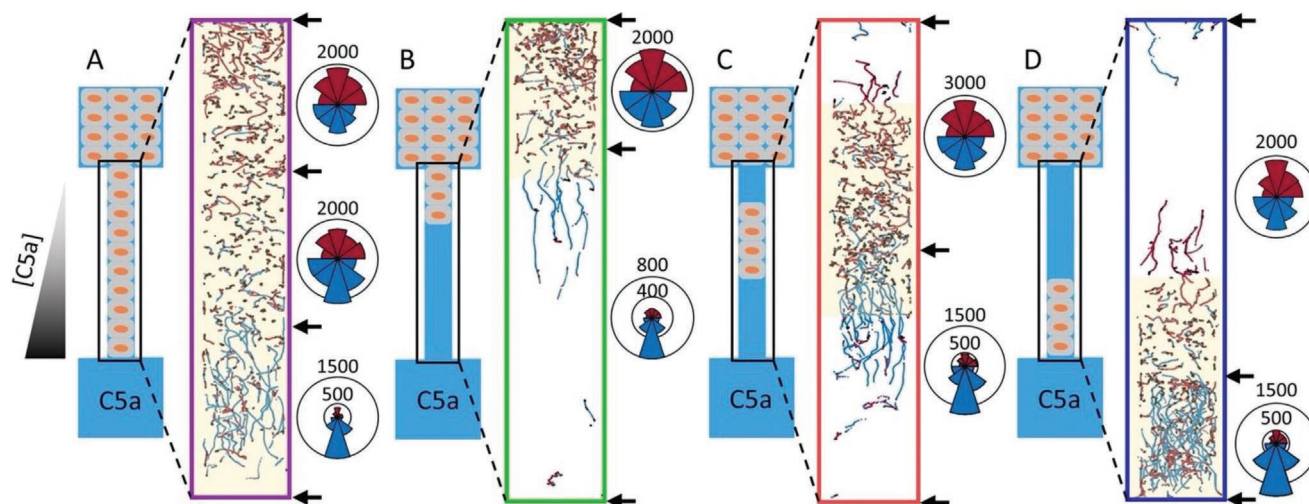


Figure 3. Patterning cells in conduits reveals unique population dynamics. BMDMs are printed in different patterns, C5a gradients established (0–10 nM), and cells imaged for 48 h. Cartoons illustrating circuits (conduit length 6 mm) plus cell starting positions, trajectories from a single experiment (blue—towards C5a, red—away from C5a, black—stationary), and rose plots (3 biological repeats; blue—towards C5a, red—away from C5a with circles indicating number of trajectory points falling into each bin) are shown at the left, right, and middle of each panel, respectively. Yellow shading: initial position of cells. A) Cells initially throughout the conduit (gradient shown). Only those at the bottom yield long blue trajectories towards C5a, and rose plots confirm this bias. B) Cells initially in the top third of the conduit respond to C5a to give long blue trajectories, and biased rose plots—in contrast to those in (i) with the same starting positions. C,D) Cells in islands initially in the middle and bottom of the conduit again show biased migration towards C5a—in contrast to those in (A) with the same starting positions.

attractant are early visible markers of chemotaxis.^[22,23] Therefore, we use our movies to trace cells yielding the long blue trajectories back in time, identify when and where they first extend pseudopodia towards attractant (Figure S3, Supporting Information), and calculate the local C5a concentration present at that time and place (using the solution to the 1D diffusion equation). Because these movies are collected using a frame rate of 20 min, temporal resolution is limited (higher frame rates can be acquired by reducing the imaged area or increasing scan rate, but then overheating can alter cell behavior and even kill cells). Therefore, we recognize the concentration, $c_{\min, \text{obs}}$, present in the earliest frame in which such pseudopodia are seen; this is an upper limit of c_{\min} . Then, in movies used for Figure 3A,D (Movies S5 and S8, Supporting Information), marker pseudopodia are seen at the bottom of the conduit in the first frame, and $c_{\min, \text{obs}}$ is ≈ 1 nM (Table 1). For movies used for Figure 3B,C (Movies S6 and S7, Supporting Information), markers are seen in the second frame, and values for $c_{\min, \text{obs}}$ are 0.1 pM and 79 pM respectively (Table 1; comparable to the minimum concentration eliciting a response in xCELLigence transwell assays, Figure S2, Supporting Information). This gives a 1000-fold range in the lowest C5a concentration eliciting a response. Values for the concentration gradients at the points

where cells respond are also given in Table 1. As these gradients are so shallow, and if a macrophage is 0.1 mm in length, this makes it likely that the first responders in Figure 3B experience a C5a concentration of c_{\min} at one end of their body and zero at the other. Such low concentrations of $c_{\min, \text{obs}}$ suggest high sensitivity of this assay, which combined with the theoretical calculations provides new ways of confidently studying chemoattractant gradients in ranges lower than previously reported.^[24,25]

2.4. Comparing Multiple Cell Types and Higher-Throughput Chemotaxis Studies in Microplates

2.4.1. Label-Free Comparison of Different Cell Populations in a Single Circuit

We next design and implement circuits with 3 chambers that enable comparison of chemotactic responses of two distinct cell populations without requiring distinguishing cell labels (Figure 4A). The middle chamber serves as a C5a reservoir, while chambers above and below contain different cell types. To establish gradients, medium is first added

Table 1. Initial response concentration and gradient for circuits in Figure 3.

	Whole	Top	Middle	Bottom
$c_{\min, \text{obs}}$ [nM]	1.01 ± 0.29	$1.2\text{e-}4 \pm 1.8\text{e-}5$	$7.9\text{e-}2 \pm 6.2\text{e-}3$	1.8 ± 0.06
Gradient [nM mm ⁻¹]	$3.1\text{e-}12 \pm 7.4\text{e-}13$	$5.9\text{e-}16 \pm 8.6\text{e-}17$	$2.52\text{e-}13 \pm 1.8\text{e-}14$	$4.9\text{e-}12 \pm 1.3\text{e-}13$

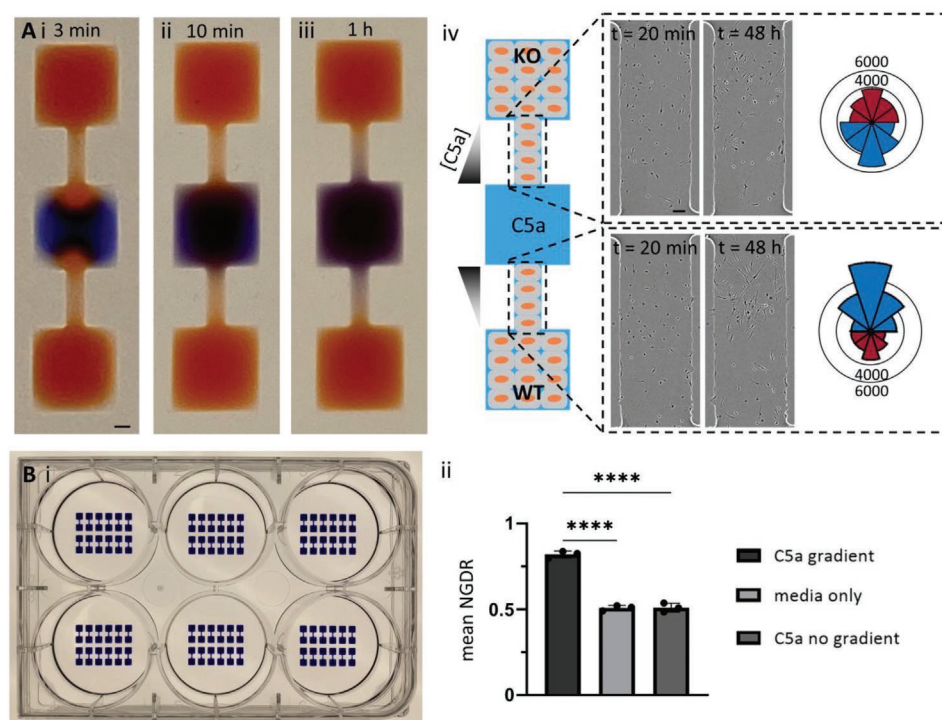


Figure 4. Comparing chemotaxis of 2 cell types in one circuit, and increasing throughput. A) Two cell types in a 3-chambered circuit. Scale bar = 500 μm . i) Images during generation of stable gradients. At $t = 0$, dyes are pipetted manually into chambers—first 1 μL red into the top chamber, 0.9 μL red into the bottom one, and finally 0.6 μL blue into the middle one. After 3 min, the induced pressure difference has driven red dye into the middle chamber, and pressures equilibrate. ii) After 10 min, blue dye has diffused throughout the middle chamber. iii) After 1 h, blue dye has diffused equally into both conduits to create steady gradients. iv) Proof-of-concept. Circuits are built around WT BMDMs in the bottom chamber, and those in which the C5a receptor is KO in the top one. Gradients are established as in (i) by adding medium \pm C5a (equivalent to red and blue dyes), and movies collected for 48 h. Insets show first and last frames, plus rose plots (3 biological replicates). WT (but not KO) cells move towards C5a. B) Increasing throughput (2-chamber circuits). i) Image of a 6-well plate containing 72 identical dumbbells (1.5 mm long conduits). Blue dye is added to aid visualization. ii) Example results. Circuits are built around WT BMDMs contained in the top chambers, and cells exposed (as Figure 2A) to 10 nM C5a added to the bottom chamber ('C5a gradient'), both chambers ('C5a no gradient'), or neither ('media only'). After collecting movies and determining trajectories, NGDRs are calculated (\pm SD, 3 biological repeats with 3 technical ones in each setup). Cells in C5a gradients yield the highest NGDRs; one-way ANOVA, statistical significance **** $P < 0.0001$.

to the top chamber (1 μL , $P_{\text{top}} = 20$ Pa), a smaller volume than the bottom one (0.9 μL , $P_{\text{bottom}} = 18.5$ Pa), and an even smaller volume of C5a to the middle one (0.6 μL , $P_{\text{middle}} = 13$ Pa). This creates pressure gradients that drive medium into the C5a chamber (Figure 4A(i)), red dye represents medium, blue represents medium + C5a until the system reaches equilibrium; then, diffusion creates a steady gradient of C5a along both conduits (Figure 4A(iii)). To demonstrate the approach, C5a-receptor 1 knock-out (KO) BMDMs are initially at the top, wild-type (WT) BMDMs at the bottom, and 10 nM C5a in the middle. As expected, KO cells exhibit mostly unbiased movement in the upper conduit (Figure 4A(iv), rose plot in top inset), as WT cells chemotax towards C5a (Figure 4A(iv), rose plot in bottom inset; Movies S9 and S10, Supporting Information). Although a small proportion of KO cells migrate directionally towards C5a, this may be due to incomplete KO of all C5a receptors in some cells or potential contribution of another receptor (C5aR2) to migratory mechanisms. This demonstrates how phenotypic differences of various cell populations can be observed and analyzed in a single microfluidic system without the need for additional labeling to distinguish subpopulations.

2.4.2. Increasing Throughput Using Microplates

We now demonstrate a method to print and operate circuits in conventional microplates to perform higher-throughput assays. The technique uses a custom-built three-axis traverse that is larger than the printer used thus far and can accommodate bigger substrates such as microplates; however, it is operated much like the printer. Then, for example, 12 identical dumbbell circuits are printed in each well of a 6-well microplate (i.e., 72 circuits in total; Figure 4B(i)). As before, gradients of chemoattractant are generated and circuits imaged to analyze cellular response. We thus compare the response of BMDMs cultured in the top chamber of circuits and exposed to gradients of C5a, to that of BMDMs plated everywhere in circuits with uniform distributions of C5a or in the absence of C5a. Results show a clear increase in the mean NGDR for cells experiencing gradients compared to controls (Figure 4B(ii), as in Figure 2D). The flexibility of the approach allows circuits with various shapes to be shrunk to fit inside wells of 12- to 96-well plates (Figure S4, Supporting Information).

2.5. Chemotaxis of BMDMs in Active (Flowing) Circuits

2.5.1. Generating an Unshifting Stable Gradient

Here, we use an 'm'-shaped circuit and infuse medium ± 10 nM C5a into left and right arms, respectively (Figure 1D). These two streams converge as laminar streams in the central arm to flow over BMDMs, and diffusion establishes a C5a gradient (from 0–10 nM) across the width of the conduit. Concentrations are determined using the solution to the 1D time-dependent diffusion equation in finite media, where $c(x,t) = \frac{c_{\max}}{2} \operatorname{erfc}\left(\frac{x}{2\sqrt{Dt}}\right)$ and t = time a molecule spends in the conduit.^[20] Flow velocities at any point in fluid-walled conduits can be predicted using a simplified power law^[26] if the geometry of the conduit footprint, flow rate, and fluid properties of perfusing medium are known. We thus determine flow velocities to transform the time-dependent diffusion solution into a distance along the device substitution using $t = \frac{x}{u}$, where u is the mean flow velocity at a given x -location.

2.5.2. BMDMs Respond to Low Concentrations of C5a in Unshifting Stable Gradients

As before, we make a movie over 48 h to follow chemotaxis of BMDMs across the central channel in the 'm'. Many migrate from the left to the center, leaving behind a cell-depleted zone (Figure 5A(i,ii); Movie S11, Supporting Information); individual trajectories and a rose plot (segment length indicates the number of trajectories per bin) confirm chemotaxis towards C5a (Figure 5A(iii)). Note that the cell band just to the right of this depleted zone is enriched in taxing cells superimposed on non-responsive ones that were initially present. A theoretical prediction of the normalized concentration gradient is now mapped onto the image of cells at 48 h (Figure 5A(iv)); colors depict local concentrations from 0 to 1 (corresponding to 0–10 nM C5a), and curves the gradient contours (red line—5 nM, with black lines correspond to decreasing concentrations). The leftmost black line is chosen to represent the minimum concentration triggering a response, and maps onto the leftmost edge of the depleted region (equivalent to $c_{\max} \times 10^{-5} = 0.1$ pM). While the diameter of a murine macrophage is typically ≈ 20 μm ,^[27] their length can be >100 μm when extending pseudopodia and moving (Figure 5A(ii)). As a result, cells in this region of the conduit easily sense one to two orders of magnitude difference in C5a concentration across their body. Remarkably, and in contrast to flow-free circuits, it is now cells far from the front that respond (as those at the front do not). We will argue in the Section, "Discussion" that this difference results from the effects of flow continually maintaining attractant levels. The predicted C5a concentrations around responsive cells in both flow-free and flowing circuits are comparable to the lowest concentrations eliciting taxis in the xCELLigence assay (Figure S2, Supporting Information), thus validating our findings. To our knowledge, the response of macrophages to such low concentrations of C5a has not been shown before.

2.5.3. Controlling Cell Movement by Shifting the Gradient

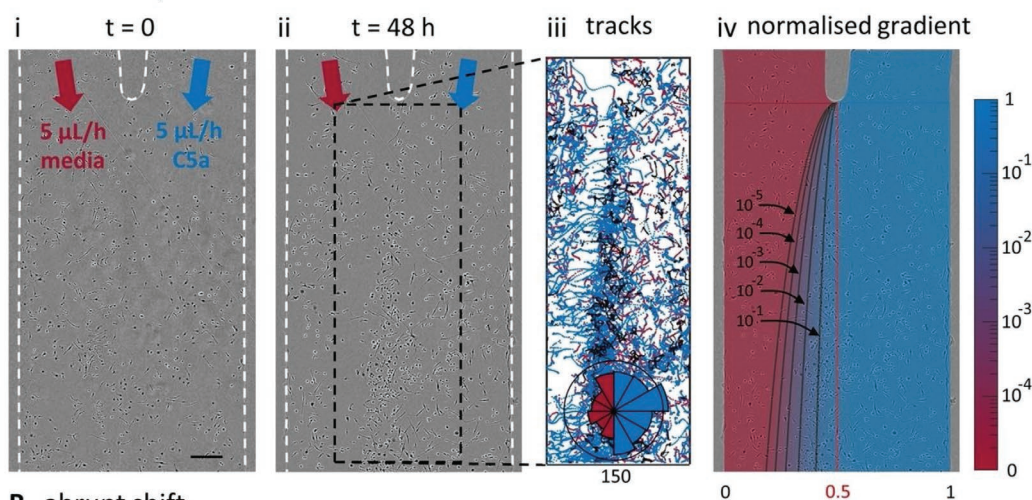
We now attempt to control cell movement by shifting the gradient a known distance to the right in order to recruit more responsive cells in specified regions of the conduit. First, a 10 nM gradient of C5a is generated over cells cultured in the conduit of an 'm'-shaped circuit as before, and cells are imaged on a microscope (Figure 5B(i)). As expected, after 24 h, a band of BMDMs has migrated into the central region of the conduit (Figure 5B(ii)). The gradient is now abruptly shifted 200 μm to the right by increasing the flow rate of the left stream (7.15 $\mu\text{L h}^{-1}$) and decreasing the flow rate of the right one (2.85 $\mu\text{L h}^{-1}$) (Figure S5, Supporting Information) as the overall flow rate in the conduit remains unchanged (10 $\mu\text{L h}^{-1}$). Cells are then imaged for an additional 24 h (Movie S12, Supporting Information). Analysis of cell trajectories and a rose plot reveals that the band of cells distributed along the center of the conduit shifts in the direction of C5a, indicating a clear bias towards the newly-positioned gradient (Figure 5B(iii,iv); note the large proportion of blue tracks towards C5a, and enlarged blue segment in the rose plot).

Since BMDMs follow a gradient of C5a when abruptly shifted, we investigate whether cells can follow a continuously-shifting gradient. As before, BMDMs are exposed to a 10 nM gradient of C5a and imaged over 24 h (as in Figure 5A), during which a subpopulation of cells migrate from the left to the center of the conduit where the concentration of C5a is higher (Figure 5C(i,ii)). Over the following 24 h, the gradient is shifted continuously from the center of the conduit to 150 μm from the right edge, by gradually increasing the flow rate through the left arm (from 5 to 9.98 $\mu\text{L h}^{-1}$) and decreasing the flow rate through the right one (from 5 to 0.02 $\mu\text{L h}^{-1}$) which is performed using the 'ramp' function of the syringe pump. Analysis of cell trajectories during this time reveals that BMDMs do not follow the gradient as efficiently, and the chemotactic bias observed previously reduces (rose plots in Figure 5C(iii)). However, when the gradient remains stationary for an additional 24 h, chemotaxis becomes stronger, and a new cell band appears on the right (Figure 5C(iv); Movie S13, Supporting Information). This confirms that cells remain competent to chemotax throughout the 72 h, and that sweeping the gradient across more cells—at least at the pace chosen in this experiment—does not significantly recruit more cells into the enriched band. To our best knowledge, the difference in macrophage response to abrupt and continuously shifting gradients has not been reported before and is a feature easily detected using our approach. This behavior is consistent with cells responding poorly when their leading edges sense falling attractant concentrations despite the presence of a gradient across their whole bodies; then, they only migrate actively once the gradient stops moving. In vivo, gradients of chemokines are likely evolving over time and therefore this new platform has the potential to facilitate our understanding of macrophage response to changing inflammatory landscape in tissues.

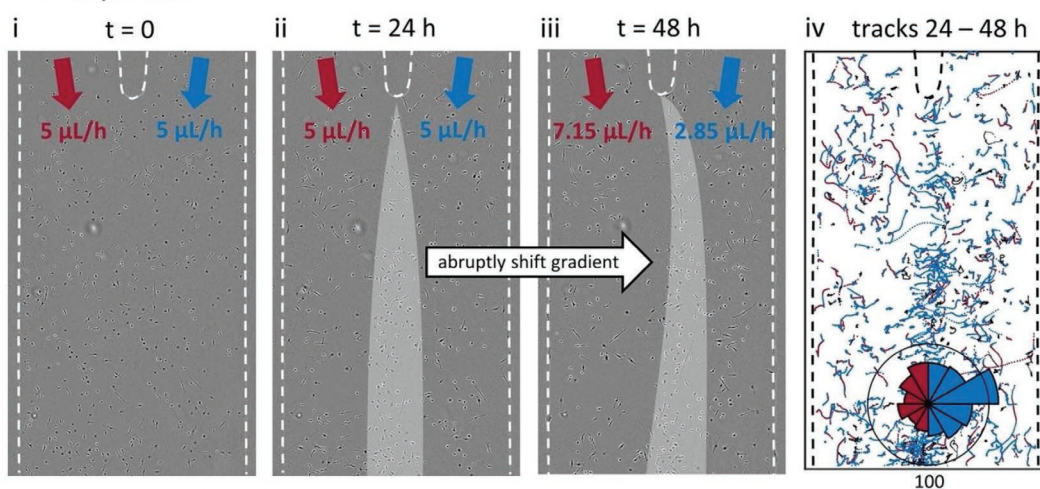
3. Discussion

We describe a suite of chemotaxis assays designed using microfluidic circuits built around living cells on standard Petri dishes

A stationary



B abrupt shift



C static, gradual shift

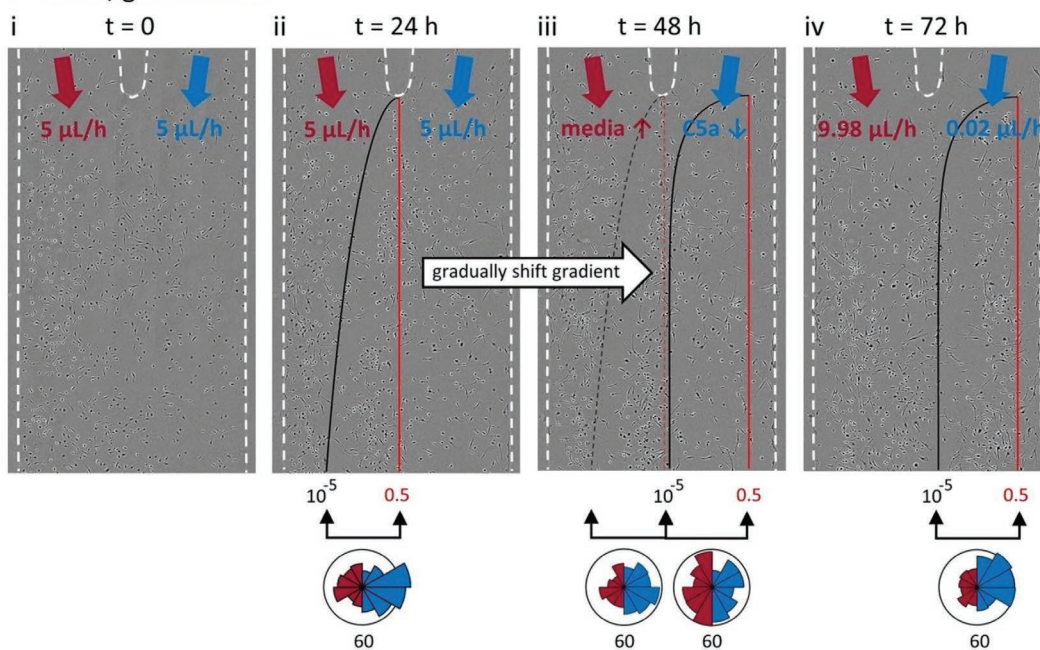


Table 2. Comparing traditional and fluid-walled chemotaxis assays.

Assay	Transwell assays	Direct observation and cell tracking chambers	Under agarose assays	Traditional microfluidic assays	Fluid-walled microfluidics
Stable gradients	+ ^[38]	+/ [−] [7,38]	−	+ ^[39,40]	+ ^[17]
Single-cell tracking	−	+ ^[31,41]	+ ^[31]	+ ^[39,40]	+ ^[28,36]
Fugetaxis detection	+ ^[42,43]	−	+ ^[44]	+ ^[45]	+ ^[17]
Distinction between chemotaxis and chemokinesis	+ ^[46]	+ ^[41,47]	+/ [−] [48]	+ ^[39,40]	+
High throughput	+/ [−] [49,50]	−	−	+ ^[13,51]	+
Specialized equipment	+/ [−] [6,50]	−	−	+ ^[39,40]	+/ [−]
Real-time observation	+/ [−] [6]	+ ^[41,47]	+ ^[31,48]	+ ^[39,40]	+ ^[17]
Multiple cell types	−	−	+/ [−] [48]	+/ [−] [51]	+
Patterning cells	−	−	−	+/ [−] [39]	+
Multiple chemoattractants	−	−	+ ^[48]	+ ^[39,51]	+
Cell isolation/circuit reconfiguration	−	−	−	−	+ ^[37]
Targeted live cell recovery	−	−	−	−	+ ^[36]

(Figure 1),^[18] and apply them to investigate the complex interactions involved in the chemotaxis of primary murine macrophages to C5a—a small peptide released at inflammation sites. Taking advantage of properties of circuits with fluid walls, this method addresses many limitations of traditional chemotaxis assays (Table 2). Gradients of C5a are established in flow-free (passive) dumbbell-shaped circuits, and theoretical models are developed to predict local C5a concentrations; as fluid walls are transparent,^[28] time-lapse movies are made, and individual cell trajectories are analyzed (Figure 2). Remarkable results are obtained by comparing responses of cells initially occupying different parts of 4 identical conduits—either the whole conduit, or just the top, middle, or bottom third. One might expect cells to respond according to position and so to predicted C5a concentration gradient; instead, responders are the ones closest to the highest C5a concentration irrespective of position (Figure 3). A proof-of-concept control in a modified 3-chamber circuit then compares the chemotactic response of WT and KO

cells (without any cell labels) and shows that WT cells migrate towards C5a more efficiently than KO ones (Figure 4A). Passive circuits are also built on well plates to increase throughput (e.g., 12 circuits in each well of a 6-well plate; Figure 4B). Finally, tenfold steeper gradients than the ones in flow-free circuits are generated with external pumps driving input flows through ‘m’-shaped circuits; now, responders are distant from the front (Figure 5A). Cell movement is also controlled by shifting gradients from the center of a conduit to the right-hand wall (by 200 or 750 μm) either abruptly or continuously (Figure 5B,C). Interestingly, cells do not efficiently follow a continuously-shifting gradient, although they do so once the gradient stops moving. In other words, cells seem to sense the presence of C5a in both time and space. In both passive and active circuits, cells respond to far lower concentrations than previously reported (≈ 0.1 pM), and this is validated using the real-time xCELLigence transwell assay (Figure S2, Supporting Information).

Figure 5. Chemotaxis in steep C5a gradients held stationary, shifted abruptly to the right, or shifted progressively to the right. BMDMs in the central conduit of ‘m’-shaped circuits are exposed to laminar streams of medium and medium + 10 nM C5a, so diffusion creates a concentration gradient across the conduit. Movies are collected as the position of this gradient is changed (either abruptly or steadily) at times indicated by varying input flows into side arms, and cell trajectories plus rose plots (segment length indicates the number of trajectory points per bin) determined (blue towards C5a, red away, black stationary). Scale bar in A(i) = 250 μm applies to all panels. Dotted white lines: fluid walls. A) Stationary gradient for 48 h (both input streams constant at 5 $\mu\text{L h}^{-1}$; 3 biological repeats). i, ii) Two movie frames illustrating views of central conduit. At $t = 0$, cells are randomly distributed; after 48 h, some cells accumulate in a vertical band (leaving a depleted region behind). iii) Cell trajectories in region indicated and the overlaid rose plot with the circle indicating the number of trajectories that fall into each bin highlights this chemotaxis. iv) Normalized concentration gradient overlaid on frame at $t = 48$ h (concentrations of 1 and 0 equal 10 and 0 nM). Contours indicate different C5a concentrations; the leftmost one marks the left of the depleted zone and so the minimum concentration inducing migration. Cells at the rear are the main responders. B) Stationary gradient for 24 h followed by an abrupt shift to the right by ≈ 200 μm , and then a stationary gradient in the new position for 24 h (equal inputs as in (A) abruptly changed after 24 h to 7.15 $\mu\text{L h}^{-1}$ on the left and 2.85 $\mu\text{L h}^{-1}$ on the right). i–iii) Movie frames. At $t = 0$ h, cells are randomly distributed. At $t = 24$ h, a central band begins to form (light-grey overlay). At $t = 48$ h, the band is further to the right (light-grey overlay). iv) Cell trajectories (24–48 h) and overlaid rose plot with the circle indicating number of trajectories falling into each bin confirm cells follow the shifted gradient. C) Gradient stationary for 24 h (equal inputs), shifted steadily by 750 μm to the right over 24 h (by progressively increasing/decreasing flows into left/right inputs), and stationary for 24 h (as existing inputs held steady). i–iv) Movie frames and rose plots with the circle indicating number of trajectories falling into each bin. Cells distributed randomly ($t = 0$), accumulate at $t = 24$ h along the centerline (red) leaving a depleted region behind (just to the right of the black line marking a concentration of 0.1 pM C5a). At $t = 48$ h, dotted and solid red/black lines indicate initial and final concentrations of 0.5 nM and 0.1 pM C5a during the intermediate phase when the gradient is shifted continuously; many cells initially in the central band remain roughly in the same position during this phase. At $t = 72$ h (and so 24 h in a steady gradient after the shift), a new band of cells accumulates close to the right-hand edge of the gradient (red line). Rose plots confirm biased cell movement towards C5a in regions indicated.

We discuss these complex results in the light of three inter-related observations. First, consider the gradients in the 4 identical passive circuits. In the absence of cells, and since all circuits have the same dimensions and contents, gradients will evolve in them identically. However, cells at equivalent points along the 4 conduits (and so experiencing similar C5a concentrations and gradients) respond in some cases, but not in others (Figure 3). Then, C5a concentration gradient cannot be the only trigger of taxis. Second, there is clear evidence that cells can distort pre-existing gradients, and even generate ones from a uniform field of attractant by binding, internalizing, or degrading attractant around them.^[29] Macrophages also change their migration when other cells further up a gradient distort the concentrations behind them.^[2,30] Moreover, self-generated gradients can guide cells robustly over longer distances than pre-existing ones, with responding cells always being the ones at the front.^[2,29] This is consistent with what we observe in flow-free gradients; taxis cells are at the front, irrespective of predicted C5a concentration (Figure 3). Third, responding cells can emit signals to near neighbors that amplify an initial response, and reduce a late one (e.g., neutrophils initially signal to each other to swarm towards infecting bacteria, and later they reduce excessive swarming and so reduce inflammation^[31]). Although such paracrine signaling has not been shown in chemotaxis macrophages, tissue-resident macrophages can coordinate extension of their pseudopodia to cloak microlesions^[32] and so must signal to each other.

It is widely accepted that eukaryotic cells regulate their responses to concentration gradients by spatial sensing.^[33] Additionally, migrating myeloid cells (dendritic cells and neutrophils) sense temporal dynamics of chemoattractant concentrations and respond to rising concentrations of CCL19 and CXCL12—a behavior that contrasts with C5a.^[34] Moreover, neutrophils migrate further towards shifting gradients of interleukin-8 than static ones.^[35] Note that there is ample time for signals to diffuse between cells in our flow-free circuits, but not in our flowing ones—as any secreted signals are quickly flushed away (e.g., in Figure 5A, medium in the conduit is wholly replaced every minute). Then, it is no longer surprising that responders are at the front in flow-free gradients (Figure 3), but not in flowing ones (Figure 5) where inter-cellular signaling becomes impossible. Therefore, our findings suggest that macrophages can sense C5a both spatially and temporally, and that shifting gradients modulate what is already a complex response.

A technical limitation of the current study results from the low temporal resolution of recordings; estimation of the minimum concentration (c_{\min}) eliciting chemotaxis in passive circuits is limited by framerate. However, our approach has various advantages; it allows users to generate stable gradients over cells freely-patterned in 2D, track individual cells, distinguish between types of movement (chemotaxis/chemokinesis), compare cells of different types without requiring additional cell labels, and—in the future—increase throughput, and isolate cells of interest in real-time for downstream analysis, as cells can be selectively retrieved through fluid walls.^[36,37] We thus hope this study provides new ways of evaluating chemotaxis and spatio-temporal sensing in adhesive mammalian cells. For example, this approach should allow comparison

of transcriptomes and proteomes of responding and non-responding cells for downstream analysis.

4. Experimental Section

Cells, Media, Culture Conditions, Reagents: C57BL/6, Balb/c or 5a1tm1Cge/J on Balb/c background (C5aR1 KO) were used in this study. C57BL/6 were bred in Oxford, the Balb/c WT plus the C5aR KO were bought from the Jackson Laboratory. To obtain BMDMs, bone marrow was extracted from femurs and tibia of mice and frozen for up to 6 months in -80°C prior to use. Upon defrosting the bone marrow was cultured for 7 days (37°C , 5% CO_2) in high-glucose Dulbecco's Modified Eagle's Medium (DMEM, Sigma) enriched with 10% L929-conditioned media (containing macrophage colony-stimulating factor), 10% Fetal Bovine Serum (FBS, Sigma) and 1% penicillin plus streptomycin (P/S, Gibco). As this combination was used throughout the study, the mixture was simply referred to as 'medium'. 8 mL medium was used for the first 4 d; then, 3 mL was removed and replaced with 5 mL fresh medium. Cells were plated on dishes on day 6, circuits built around them on the same or next day for passive and active circuits, respectively, and chemoattractants added on day 7. Most circuits were built on 35 mm Petri dishes (Corning, 430165) or 6-well plates (Corning, 3516). 12- to 96-well microplates were additionally used (Corning) for higher-throughput applications. In all chemotaxis assays, recombinant mouse complement component 5a was used (C5a, 10 nM; R&D Systems).

Imaging: BMDMs were imaged at a rate of 3 frames h^{-1} (for experiments in dishes) or 2 frames h^{-1} (for experiments in plates) using an InCuCyte ZOOM, a live-cell imaging system (Sartorius, Göttingen, Germany). The InCuCyte was itself contained in an incubator (37°C , 5% CO_2).

Printing Circuits: In all experiments, cells were first plated on either Petri dishes or microplates, and—after attaching to the substrate—the circuit was jetted around them. Cell plating and circuit printing were performed on custom-made three-axis traverses (iotaSciences Ltd, Oxford, UK) referred to as a 'printer' (for circuits on Petri dishes), and larger 'pro-printer' (for circuits on microplates).

Loading and Patterning Cells: Cells were first plated on the dish using the printer.^[18] Briefly, the three-axis arm of the printer holds a dispensing needle (25G, Adhesive Dispensing Ltd) connected by PTFE tubing (Cole-Parmer) to a 250 μL glass syringe (Hamilton) controlled by a syringe pump (iotaSciences Ltd). The needle was brought 300 μm above the dish surface and infuses BMDMs in medium + 2% fibronectin (Sigma, F1141; 1 million cells mL^{-1}). The needle was then moved over the surface of the dish to deposit cells in the desired pattern. After printing, the dish was incubated (5 min) to allow cells to attach.

Jetting Circuits: The dish was now removed from the incubator and 1 mL medium was gently added to wet the entire bottom. Most medium was removed, and 1 mL FC40 (iotaSciences Ltd) was added to cover the remaining thin film of medium. The dish was placed back on the printer in the same orientation and a second needle loaded with FC40 jets a stream of FC40 vertically downwards from 500 μm above the surface of the dish. When this jet contacts the surface, it displaces the underlying medium, and—as FC40 wets polystyrene better than water—it replaces medium to form a fluid wall (a medium:FC40 interface). The needle was then moved over the dish and around cells to create fluid walls that form the footprint of the circuit.^[18] For passive circuits, 1 μL medium was initially added to each chamber after jetting the circuit.

Circuit Design: Two types of circuit were used, static (passive) circuits without flow, and dynamic (active) ones with flow. The first passive circuits used were dumbbell-shaped and consist of two square chambers (footprints 2.5×2.5 mm) connected by a thin conduit (600 μm wide, 1.5 mm long). Circuits were built around cells so cells end up in the top chamber, in the top chamber + conduit, or in bands at different positions in the conduit. C5a was then added to the bottom chamber. For these experiments, 12 circuits were printed in each dish (Figure 1C). Cells in different locations of the circuit grow under different heights of medium due to the curved profile of the overlying fluid interface,

and this might affect cell behavior; therefore, cells growing at different positions were tracked throughout static circuits in medium or a uniform distribution of C5a (i.e., without a gradient), and find that average cell velocities were unaffected by position in the circuit (Figure S8, Supporting Information).

For cell-comparison studies (Figure 4A), a slightly modified version of the passive circuit was used by connecting three chambers (also 2.5 mm wide) to two conduits (600 μm wide, 1.5 μm long). Due to larger circuit sizes, 6 circuits were printed in each dish.

For flow-generated gradients, 'm'-shaped circuits were used. These circuits consist of two arms that join into a conduit that ends in a large circular sink (7 mm wide). Cells grow in the central conduit (6 mm long, 1.8 mm wide), and side arms were used to perfuse medium or medium + C5a.

Passive Circuit: As described previously, reagents were loaded using the printer, and dishes subsequently moved to the IncuCyte for imaging. Loading was performed by matching reagent volumes to ensure that C5a remains in the bottom chamber and does not flow into the conduit. To achieve this, pressure in the C5a chamber was kept lower than the medium chamber during loading, so medium flows into the C5a chamber until the system reaches equilibrium and then diffusion can create a steady gradient down the conduit. This was done by first infusing 1 μL medium into the top chamber, and then 0.5 μL C5a in the bottom chamber. After loading all 12 circuits, the dish was gently moved from printer to incubator (to not cause sudden flows of C5a) and placed inside the IncuCyte for imaging.

Active Circuit: Gradients in active circuits were generated as in previous studies.^[17] Briefly, two 500 μL glass syringes (Hamilton) were loaded with either medium or medium + 10 nM C5a, placed on a syringe pump (Harvard Apparatus), and connected to needles via PTFE tubing. Using a 3D printed adaptor that fits around the edge of the dish and holds the needles, needles were inserted into each arm of the circuit (left—medium, right—C5a). A third needle—also connected to a 1 mL glass syringe (Hamilton) on a separate syringe pump and held in the adaptor—was inserted into the sink. The first two needles were set to infuse (at rates indicated in Figure 5; total flow rate in the conduit is always 10 $\mu\text{L h}^{-1}$), while the third needle withdraws at an equivalent flow rate (10 $\mu\text{L h}^{-1}$). The circuit was overlaid with an additional 4 mL of FC40, and placed inside the IncuCyte to begin imaging.

Determining the Diffusion Coefficient of C5a: In both types of circuits, theoretical models were used to predict local concentrations and gradient steepness across conduits. The models use well-known solutions to the 1D diffusion equation (Supporting Information) that require the diffusion coefficient of C5a to be known. D_{C5a} was thus determined using the Stokes–Einstein equation for the diffusion of a spherical particle in water of radius r as $D = \frac{k_B T}{6\pi\eta r}$ (k_B = Boltzmann's

constant, T = absolute temperature, η = dynamic viscosity). The Stokes radius of a C5a molecule was first determined using its molecular weight, $M_{\text{C5a}} = 9 \text{ kDa}$, as $r = 1.82 \text{ nm}$. Then, using $\eta_{\text{water}} = 0.7 \text{ cP}$ and $T = 310.15 \text{ K}$ (37 $^{\circ}\text{C}$), $D_{\text{C5a}} = 1.8 \times 10^{-10} \text{ m}^2 \text{ s}^{-1}$ was found.

xCELLigence Chemotaxis Assay: Real-time xCELLigence chemotaxis assays were performed as previously described.^[6] Briefly, CIM-16 plates were used in RTCA-DP instrument (Agilent, Santa Clara, USA). Experimental concentrations (0.003 pM–300 nM) of C5a were re-suspended in chemotaxis buffer (RPMI-1640 + 25 mM HEPES solution + 0.5% bovine serum albumin) and 160 μL of pure chemotaxis medium or the C5a solution were placed in the bottom chamber of the CIM-16 plates. The top insert was then attached and 50 μL of pure chemotaxis buffer was added to the top chamber; the plates were left in the incubator for 30 min to allow gradient formation. BMDMs were re-suspended at $2 \times 10^6 \text{ cells mL}^{-1}$ in chemotaxis buffer. After 30 min, a blank recording was taken and 50 μL BMDM suspension was added to the top chamber. Cells were left at room temperature for 10 min to attach after which recording starts, and measurements were taken every 40 s. RPMI-1640 was bought from Gibco, HEPES solution and bovine serum albumin were bought from Sigma. Traces of the impedance measurements were registered every 40 s for 4 h with 2 technical repeats for each trace.

Traces were normalized to baseline migration for each CIM-16 plate (cell impedance measured for wells with pure media and no C5a gradient) and then averaged. The area under the curve (AUC) was quantified for each trace ($n = 3\text{--}7$ biological repeats per concentration) \pm SEM.

Image Analysis: To analyze and quantify migration of individual macrophages, thousands of cells were found using a custom-made particle-tracking algorithm in Fiji. Briefly, bright-field images were extracted, stabilized, the median background intensity subtracted, and particle locations recorded. Analyses of trajectories to quantify cell velocities, NGDR, and chemotactic bias were then performed in Matlab as previously described.^[21]

Statistical Analysis: All experiments were designed, where possible, to generate groups of equal size. Where possible, blinding and randomization protocols were used. All data in the text and figures were presented as mean \pm standard deviation (SD) or \pm standard error mean (SEM), as indicated in the figure legend, of n observations carried across at least 2 independent experiments, where n represents the number of biological repeats or independent values, not technical replicates. Statistical analysis was calculated using GraphPad Prism 9 (GraphPad Software, San Diego, California, USA; RRID:SCR_002798). Normally distributed data without repeated measurements were assessed by a one-way ANOVA followed by Turkey post-hoc test; in all cases a $P < 0.033$ was considered significant.

Supporting Information

Supporting Information is available from the Wiley Online Library or from the author.

Acknowledgements

The authors thank Richard Wheeler for help with the cell tracking in Fiji. This work was supported by IotaSciences Ltd. (who provided a scholarship for C.D. and F.N.), the Impact Acceleration Account of the Biotechnology and Biological Sciences Research Council (P.R.C. and E.J.W.), awards from the Medical Research Council under the Confidence in Concept scheme (MC_PC_15029 to P.R.C. and E.J.W.). Research in the Greaves laboratory is funded by the British Heart Foundation (BHF) RG/15/10/3148 and A.N.R. is the recipient of a BHF graduate studentship FS/17/68/33478. J.H.R.W. acknowledges funding from the Biotechnology and Biological Sciences Research Council (BB/R018383/1).

Note: The presentation of the third sentence in the abstract was changed on September 9, 2022, after initial publication online.

Conflict of Interest

P.R.C. and E.J.W. each hold equity in and receive emoluments from IotaSciences Ltd., a company exploiting the fluid-shaping technology; IotaSciences Ltd. also provided the printers, the FC40STAR, and a scholarship for C.D. All other authors declare they have no competing interests.

Author contributions

C.D. and A.N.R. contributed equally. C.D., A.N.R., P. R.C., D.R.G., and E.J.W. designed the research; C.D., A.N.R., and F.N. performed experiments; C.D., A.N.R., and J.H.R.W. analyzed data; and all authors worked on the paper.

Data Availability Statement

The data that support the findings of this study are available in the supplementary material of this article.

Keywords

cell patterning, fluid walls, macrophage chemotaxis, microfluidics

Received: February 23, 2022

Revised: April 18, 2022

Published online: July 19, 2022

- [1] D. M. Mosser, K. Hamidzadeh, R. Goncalves, *Cell. Mol. Immunol.* **2020**, *18*, 579.
- [2] G. E. Jones, *J. Leukocyte Biol.* **2000**, *68*, 593.
- [3] Y. V. Bobryshev, E. A. Ivanova, D. A. Chistiakov, N. G. Nikiforov, A. N. Orekhov, *Biomed Res. Int.* **2016**, *2016*, 9582430.
- [4] S. Gencer, B. R. Evans, E. P. C. Van Der Vorst, Y. Döring, C. Weber, *Cells* **2021**, *10*, 226.
- [5] S. Boyden, *J. Exp. Med.* **1962**, *115*, 453.
- [6] A. J. Iqbal, D. Regan-Komito, I. Christou, G. E. White, A. Kenyon, L. Taylor, T. S. Kapellos, E. A. Fisher, K. M. Channon, D. R. Greaves, *PLoS One* **2013**, *8*, e58744.
- [7] D. Zicha, G. A. Dunn, A. F. Brown, *J. Cell Sci.* **1991**, *99*, 769.
- [8] F. Vianello, E. Righi, M. C. Poznansky, in *T-Cell Trafficking: Methods and Protocols*, (Eds.: F. M. Marelli-Berg, S. Nourshargh), Humana Press, Totowa, NJ **2010**, p. 115.
- [9] H. Harris, *Physiol. Rev.* **1954**, *34*, 529.
- [10] W. Zhao, H. Zhao, M. Li, C. Huang, *J. Transl. Med.* **2020**, *18*, 168.
- [11] D. Irimia, *Annu. Rev. Biomed. Eng.* **2010**, *12*, 259.
- [12] C. Frick, P. Dettinger, J. Renkawitz, A. Jauch, C. T. Berger, M. Recher, T. Schroeder, M. Mehling, *PLoS One* **2018**, *13*, e0198330.
- [13] Z. Xu, P. Fang, B. Xu, Y. Lu, J. Xiong, F. Gao, X. Wang, J. Fan, P. Shi, *Nat. Commun.* **2018**, *9*, 4745.
- [14] M. Samandari, L. Rafiee, F. Alipanah, A. Sanati-Nezhad, S. H. Javanmard, *Sci. Rep.* **2021**, *11*, 10310.
- [15] E. Berthier, E. W. Young, D. Beebe, *Lab Chip* **2012**, *12*, 1224.
- [16] S. Halldorsson, E. Lucumi, R. Gómez-Sjöberg, R. M. T. Fleming, *Biosens. Bioelectron.* **2015**, *63*, 218.
- [17] E. J. Walsh, A. Feuerborn, J. H. R. Wheeler, A. N. Tan, W. M. Durham, K. R. Foster, P. R. Cook, *Nat. Commun.* **2017**, *8*, 816.
- [18] C. Soitu, N. Stovall-Kurtz, C. Deroy, A. A. Castrejón-Pita, P. R. Cook, E. J. Walsh, *Adv. Sci.* **2020**, *7*, 2001854.
- [19] R. R. Kew, in *Pathobiology of Human Disease*, (Eds.: L. M. McManus, R. N. Mitchell), Academic Press, San Diego **2014**, p. 231.
- [20] J. Crank, *The Mathematics of Diffusion*, Clarendon Press, Oxford **1975**.
- [21] N. M. Oliveira, K. R. Foster, W. M. Durham, *Proc. Natl. Acad. Sci. USA* **2016**, *113*, 6532.
- [22] W. E. Allen, G. E. Jones, J. W. Pollard, A. J. Ridley, *J. Cell Sci.* **1997**, *110*, 707.
- [23] R. R. Kay, P. Langridge, D. Traynor, O. Hoeller, *Nat. Rev. Mol. Cell Biol.* **2008**, *9*, 455.
- [24] H. O. J. Morad, S. C. Belete, T. Read, A. M. Shaw, *J. Immunol. Methods* **2015**, *427*, 13.
- [25] A. Sagar, W. Dai, M. Minot, R. LeCover, J. D. Varner, *PLoS One* **2017**, *12*, e0187373.
- [26] C. Deroy, N. Stovall-Kurtz, F. Nebuloni, C. Soitu, P. R. Cook, E. J. Walsh, *Microsyst. Nanoeng.* **2021**, *7*, 93.
- [27] D. A. Guertin, D. M. Sabatini, *eLS* **2006**, <https://doi.org/10.1038/npg.els.0003359>.
- [28] C. Soitu, C. Deroy, A. A. Castrejón-Pita, P. R. Cook, E. J. Walsh, *SLAS Technol.* **2019**, *25*, 267.
- [29] L. Tweedy, O. Susanto, R. H. Insall, *Curr. Opin. Cell Biol.* **2016**, *42*, 46.
- [30] S. E. Webb, J. W. Pollard, G. E. Jones, *J. Cell Sci.* **1996**, *109*, 793.
- [31] K. Kienle, K. M. Glaser, S. Eickhoff, M. Mihlan, K. Knöpper, E. Reátegui, M. W. Eppel, M. Gunzer, R. Baumeister, T. K. Tarrant, R. N. Germain, D. Irimia, W. Kastenmüller, T. Lämmermann, *Science* **2021**, *372*, eabe7729.
- [32] S. Uderhardt, A. J. Martins, J. S. Tsang, T. Lämmermann, R. N. Germain, *Cell* **2019**, *177*, 541.
- [33] C. A. Parent, P. N. Devreotes, *Science* **1999**, *284*, 5415.
- [34] C. E. Petrie Aronin, Y. M. Zhao, J. S. Yoon, N. Y. Morgan, T. Prüstel, R. N. Germain, M. Meier-Schellersheim, *Immunity* **2017**, *47*, 862.
- [35] M. A. Qasaimeh, M. Pyzik, M. Astolfi, S. M. Vidal, D. Juncker, *Adv. Biosyst.* **2018**, *2*, 1700243.
- [36] C. Soitu, et al., *Proc. Natl. Acad. Sci. USA* **2018**, *115*, E5926.
- [37] C. Soitu, A. Feuerborn, C. Deroy, A. A. Castrejón-Pita, P. R. Cook, E. J. Walsh, *Sci. Adv.* **2019**, *5*, 6.
- [38] D. A. Lauffenburger, S. H. Zigmond, *J. Immunol. Methods* **1981**, *40*, 45.
- [39] J. Schwarz, et al., *Sci. Rep.* **2016**, *6*, 36440.
- [40] E. van den Bos, S. Walbaum, M. Horsthemke, A. C. Bachg, P. J. Hanley, *JoVE* **2020**, *158*, e60750.
- [41] A. P. Wheeler, C. M. Wells, S. D. Smith, F. M. Vega, R. B. Henderson, V. L. Tybulewicz, A. J. Ridley, *J. Cell Sci.* **2006**, *119*, 2749.
- [42] P. Ogilvie, S. Paoletti, I. Clark-Lewis, M. Uguccioni, *Blood* **2003**, *102*, 789.
- [43] P. M. Cano, A. Vargas, J.-P. Lavoie, *BioTechniques* **2016**, *60*, 245.
- [44] J. E. Phillips, R. H. Gomer, *Proc. Natl. Acad. Sci. USA* **2012**, *109*, 10990.
- [45] W. G. Tharp, R. Yadav, D. Irimia, A. Upadhyaya, A. Samadani, O. Hurtado, S.-Y. Liu, S. Munisamy, D. M. Brainard, M. J. Mahon, S. Nourshargh, A. van Oudenaarden, M. G. Toner, M. C. Poznansky, *J. Leukocyte Biol.* **2006**, *79*, 539.
- [46] H. M. Buettner, D. A. Lauffenburger, S. H. Zigmond, *J. Immunol. Methods* **1989**, *123*, 25.
- [47] W. E. Allen, D. Zicha, A. J. Ridley, G. E. Jones, *J. Cell Biol.* **1998**, *141*, 1147.
- [48] Y. Mousseau, D. Leclers, K. Faucher-Durand, J. Cook-Moreau, A.-S. Lia-Baldini, M. Rigaud, F. G. Sturtz, *BioTechniques* **2007**, *43*, 509.
- [49] W. Falk, R. H. J. Goodwin, E. J. Leonard, *J. Immunol. Methods* **1980**, *33*, 239.
- [50] L. Taylor, M. H. Brodermann, D. McCaffary, A. J. Iqbal, D. R. Greaves, *PLoS One* **2016**, *11*, e0160685.
- [51] J. Wu, A. Kumar-Kanojia, S. Hombach-Klonisch, T. Klonisch, F. Lin, *Lab Chip* **2018**, *18*, 3855.



Supporting Information

for *Adv. Mater. Technol.*, DOI: 10.1002/admt.202200279

Assaying Macrophage Chemotaxis Using Fluid-Walled Microfluidics

Cyril Deroy, Agata N. Rumianek, James H. R. Wheeler, Federico Nebuloni, Peter R. Cook, David R. Greaves, and Edmond J. Walsh**

Supporting Information

Assaying macrophage chemotaxis using fluid-walled microfluidics

Cyril Deroy, Agata N. Rumianek, James H. R. Wheeler, Federico Nebuloni, Peter R. Cook, David R. Greaves*, Edmond J. Walsh*

Determining concentration gradients in passive circuits

The dumbbell-shaped passive circuits consist of two square chambers connected by a thin conduit (**Materials and Methods**). Shortly after adding C5a in the bottom chamber, the system reaches equilibrium (no pressure gradient) and diffusion creates a concentration gradient of C5a across the conduit. Diffusion is described by Fick's second law as $\frac{\partial c}{\partial t} = D \frac{\partial^2 c}{\partial x^2}$ (c = concentration, t = time, x = distance, D = diffusion coefficient). The concentration gradient in the conduit is expressed by the solution to the one-dimensional diffusion equation for a semi-infinite medium with constant concentration c_{max} at the boundary^[20]:

$$c(x, t) = c_{max} \operatorname{erfc} \left(\frac{x}{2\sqrt{Dt}} \right) \#(S1)$$

From Eq. S1, we determine the time for the system to reach steady state, which we define as 15% of the initial concentration c_{max} reaching the end of the conduit, $t_{ss} = \frac{x^2}{4D \times \operatorname{erfc}^{-1}(0.15)^2}$, with x = conduit length. After this time, the gradient is linear and set to vary from 0 to 10 nM. We then assess how long concentration gradients remain stable to determine maximum experimental runtimes, t_{end} . We define t_{end} as the time taken for the concentration in the media chamber to reach 5% of the initial concentration c_{max} in the C5a-free chamber where it becomes evenly distributed ($c_{end} = 0.05 \times c_{max}$ @ t_{end}). To evaluate t_{end} , we determine the rate of mass transfer through a conduit using Fick's first law of diffusion which gives:

$$\dot{m} = -DA \frac{dc}{dx} \#(S2)$$

Hence once we know the mass of C5a to be transferred, we determine t_{end} as:

$$t_{end} = 1.05 \frac{x_{conduit} m_{c5a_{transferred}}}{DA_{conduit} c_{max}} \#(S3)$$

The cross-sectional area of the conduit, $A_{conduit}$, is now determined to find t_{end} . As the system is static, Laplace pressure (ΔP) in the circuit is equal everywhere such that $\Delta P_{chamber} = \Delta P_{conduit}$, with $\Delta P_{chamber} = \frac{2\gamma}{R_{chamber}}$ and $\Delta P_{conduit} = \frac{\gamma}{R_{conduit}}$ (R = radius of curvature); thus, $R_{chamber} = 2R_{conduit}$ (**Figure S1**).

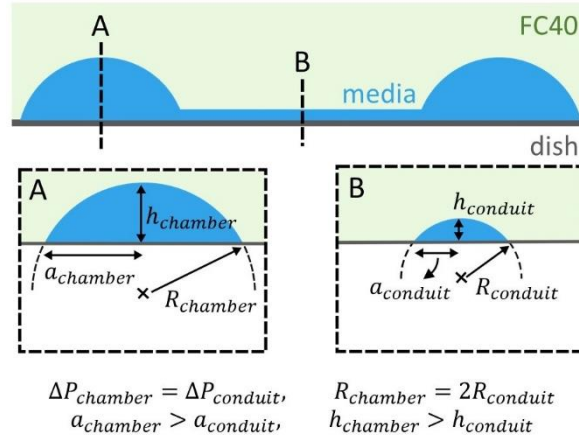


Figure S1. Geometrical properties of passive circuits. The top panel illustrates a side view of a dumbbell circuit consisting of two large chambers with spherical caps connected by a thin conduit. The bottom-left panel shows the cross-sectional profile of the chamber at A, while the bottom-right panel illustrates the conduit cross-section at B.

Heights of sessile drops are determined from their volume using $V = \frac{\pi h}{6} (3a^2 + h^2)$.^[17] To determine heights in our chambers with square footprints, we assume their pressure is equivalent to circular chambers with the same radius a . Thus, rearranging the terms of the previous equation:

$$h_{chamber} = \frac{\left(\sqrt{\pi^2 a_{chamber}^6 + 9V_{chamber}^2} + 3V_{chamber} \right)^{\frac{2}{3}} - \pi^{\frac{2}{3}} a_{chamber}^2}{\sqrt[3]{\pi} \sqrt[3]{\sqrt{\pi^2 a_{chamber}^6 + 9V_{chamber}^2} + 3V_{chamber}}}$$

Since $R_{chamber} = 2R_{conduit}$ and $R = \frac{a^2 + h^2}{2h}$, $h_{conduit}$ is expressed in terms of $h_{chamber}$ as:

$$h_{conduit} = \frac{a_{chamber}^2 + h_{chamber}^2 - \sqrt{a_{chamber}^4 + h_{chamber}^4 - 16a_{conduit}^2 h_{chamber}^2 + 2a_{chamber}^2 h_{chamber}^2}}{4h_{chamber}}$$

To validate our assumption, we measure $h_{conduit}$ in passive circuits with square and circular chambers of equivalent radii, $a_{chamber}$, using fluorescent beads as described previously.^[25] Using $V_{chamber} = 1.75 \mu\text{L}$ (the volume used in this study), we find good agreement between theoretical and measured heights (i.e., $h_{conduit, theoretical} = 65 \mu\text{m}$, $h_{conduit, square} = 65.7 \pm 6 \mu\text{m}$, $h_{conduit, circular} = 68.6 \pm 2 \mu\text{m}$). We then calculate steady-state and maximum experimental runtimes for circuits of varying lengths, summarized in **Table S1**:

Table S1. Steady-state times and maximum runtimes in passive circuits

Conduit length (mm)	1.5	2	3	4	5	6	7
t_{ss} (h)	0.9	1.5	3.4	6	9.5	13.6	18.6
t_{end} (d)	11.5	15	23	30	38	45	53

Dose-response of BMDMs to C5a

To determine the concentration of C5a eliciting the strongest migration response, we perform xCELLigence chemotaxis assays to establish a dose-response curve (**Figure S2**). From these measurements, we find that BMDM response to C5a has a skewed ball-shaped curve and that 10 nM C5a elicits the strongest response, and this concentration is used throughout in all experiments.

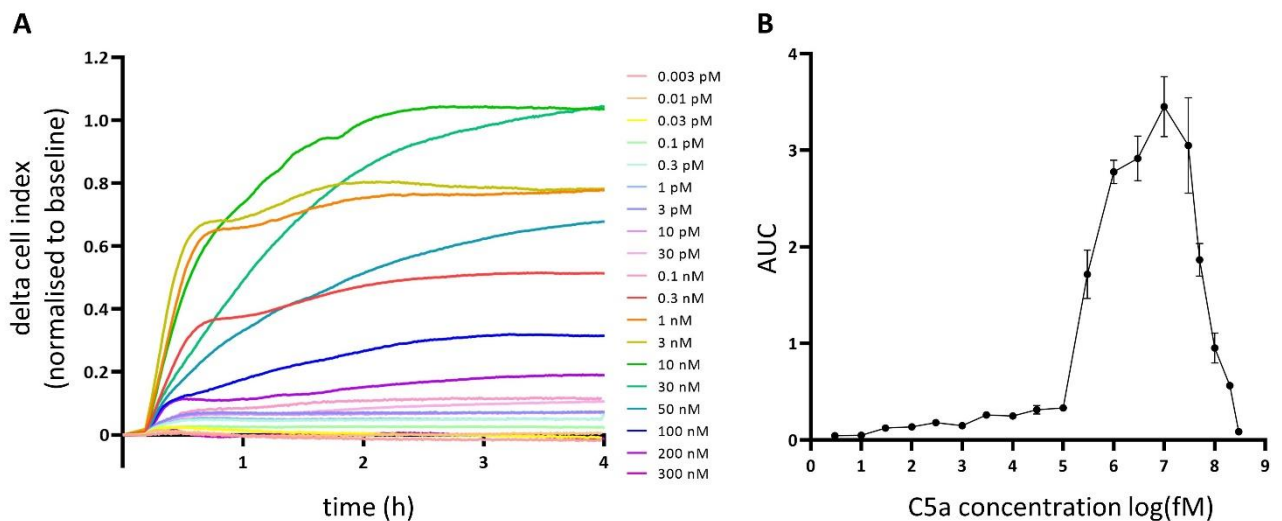


Figure S2. BMDM dose-response to C5a. A real-time xCELLigence assay (modified transwell assay) is used to perform dose-response measurements of BMDMs to concentrations of C5a ranging from 0.003 pM – 300 nM. **(A)** Mean traces of the impedance measurements registered every 40 seconds for 4 hours are normalized to baseline for each CIM-16 plate (cell impedance measured for wells with pure media and no C5a gradient). **(B)** The area under the curve (AUC) is quantified for the traces in A ($n = 3-7$ biological repeats per each concentration, error bars = SEM which are sometimes too small to be seen with AUCs <1).

Determining chemotaxis onset in passive circuits

To determine the onset of chemotaxis, we analyze morphological changes in BMDMs that are characteristic of cell migration. As BMDMs extend pseudopodia to move across surfaces and sense chemical stimuli^[51], we determine the time required for these pseudopodia to become apparent around cells (**Figure S3**). This time then provides a window during which cells are activated, and corresponding concentrations and gradient strengths are determined using the distance of cells to the C5a chamber.

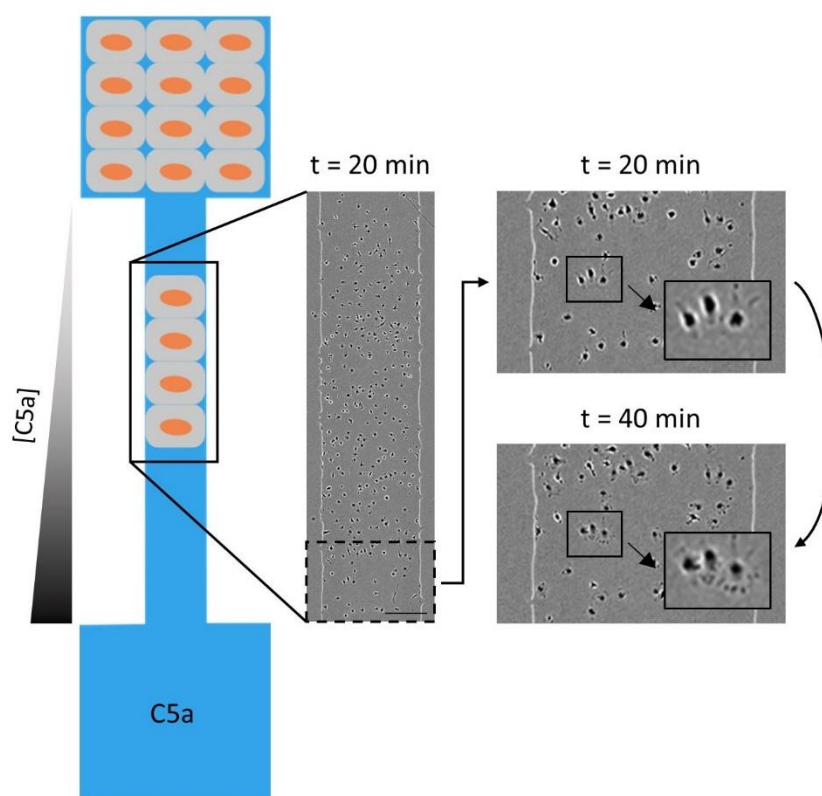


Figure S3. Chemotaxis onset in passive circuits. The cartoon (left) shows the experimental setup in Figure 4iii. The central image is from the first frame in the movie ($t = 20$ min after C5a addition) and shows the part of the conduit containing cells. Inset at top right illustrates a close-up of cells that will chemotax

over the next 2 days; they are mostly round. Inset at bottom right shows the same region in the next frame ($t = 40$ min); pseudopodia are now visible extending from rounded cell bodies. Scale bar: 250 μm .

Flexible circuit designs in microplates

This approach gives users great flexibility in designing and implementing circuits that fit other well-plate formats, for example, if they wish to compare more cell types or increase throughput. For instance, the comparison circuit of **Figure 4A** can be modified to add two additional chambers and conduits, allowing comparison of response of four different cell types to one attractant, without requiring additional cell labels (**Figure S4**). By tuning circuit size, higher-throughput comparisons can be performed on 6, 12, 24 and 48-wellplates (**Figure S4ii-v**; circuits filled with alternating blue and red dyes). Circuits can also be shrunk to fit inside each well of a 96-wellplate, and we illustrate this by printing a series of dumbbell circuits with increasing numbers of interconnecting conduits (1 – 8 conduits from top to bottom in the last panel of **Figure S4vi**).

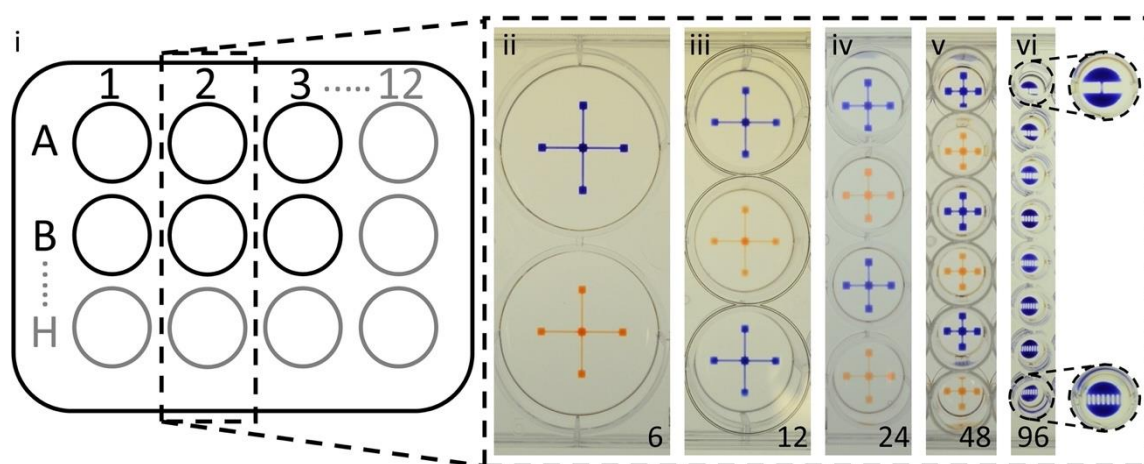


Figure S4. Printing circuits for higher throughput in well plates. Increasing throughput with chambers allowing comparison of up to 4 cell types. (i) Cartoon illustrates one column from plates with 6 to 96 wells, and images show a column from each plate. (ii-v) In 6- to 48-well plates, circuits have 5 chambers and conduit length decreases as wells become smaller. (vi) In the 96-well plate, each circuit has 2 chambers with 1-8 connecting conduits. Insets show zoom of rows 1 and 8.

Determining concentration gradients in active circuits

To predict concentration gradients in active circuits, we use the solution to the one-dimensional diffusion equation in which the initial distribution of diffusing substance

occupies a finite region and the initial state is defined by $c = c_{max}, x < 0, c = 0, x > 0, t = 0$, given by ^[20]:

$$c(x, t) = \frac{c_{max}}{2} \operatorname{erfc}\left(\frac{x}{2\sqrt{Dt}}\right) \#(S4)$$

In this case, time is transformed into distance along the conduit using the mean flow velocity. Unlike traditional microfluidic devices with fixed geometries, fluid-walled conduits have flexible interfaces that morph with changes in pressure; as a result, conduit height decreases in the flow direction due to decreasing pressure. Furthermore, conduits have cross-sections that are sections of a circle (**Figure S5A**). Thus, the average velocity in a conduit will vary as a function of conduit length, x , and conduit width, z . ^[25] To predict the shape of the concentration gradient in conduits where streams meet along the conduit centerline (i.e., $Q_1 = Q_2$, **Figure S5Bi**), we determine the average velocity, u_{mean} , along the centreline (red line in **Figure S5Bi**) over the entire conduit length (in increments $\Delta x = 6 \mu\text{m}$). From these values, we infer the time t a particle spends in the conduit at a given x -location as $t = \frac{x}{u_{mean}}$ and substitute this in Eq. S4 to obtain the local concentration.

As discussed in **Figure 5**, gradients can be shifted by varying the ratio of flow rate between input streams Q_1 and Q_2 (**Figure S5B**). Using the previously established semi-analytical solution to predict conduit heights in flowing systems ^[25], we now apply the solution to determine flow rate ratios required to shift gradients by a fixed distance (red line in **Figure S5Bii**). First, using the total flow rate in the conduit (i.e., $Q_{total} = Q_1 + Q_2$; in this study we set $Q_{total} = 10 \mu\text{L/h}$), we determine the maximum conduit height, h_{max} , and velocity, u_{max} , for a conduit of length L using $h_{max} = \left(\frac{26.08Q_{total}\mu\text{aL}}{\gamma}\right)^{0.25}$ and $u_{max} = \frac{Q_{total}}{0.61h_{max}a}$ (μ = viscosity, a = conduit half-width, γ = interfacial tension). Since Q_{total} can be expressed in terms of h_{max} and u_{max} as $Q_{total} = \frac{2}{3} \frac{u_{max}}{h_{max}^2} \int_0^{2a} h_z^3 dz$, where h_z corresponds to height across the conduit width, we next determine Q_1 and Q_2 to position the gradient at location s across the width of the conduit using:

$$Q_1 = \frac{2}{3} \frac{u_{max}}{h_{max}^2} \int_0^s h_z^3 dz \#(S5)$$

$$Q_2 = \frac{2 u_{max}}{3 h_{max}^2} \int_s^{2a} h_z^3 dz \quad \#(S6)$$

Thus, the position of the gradient can be shifted to any location across the conduit using these sets of equations to determine the necessary flow rate ratios. Note that the same principle can also be applied for increasing numbers of input streams. Since shifting gradients brings the centerline closer to the conduit edge where flow velocities are lower due to conduit curvature, we adapt our model to account for these changing velocities. We first begin by predicting t using the mean velocity at the new shifted location, $u_{mean\ shift}$. Then, moving down the conduit in steps Δx as before, we incrementally shift the mean velocity used to calculate t in steps Δz ($u_{mean\ shift-\Delta z}$), in the direction of the conduit centreline (i.e., $\Delta z = L/(s - a)$).

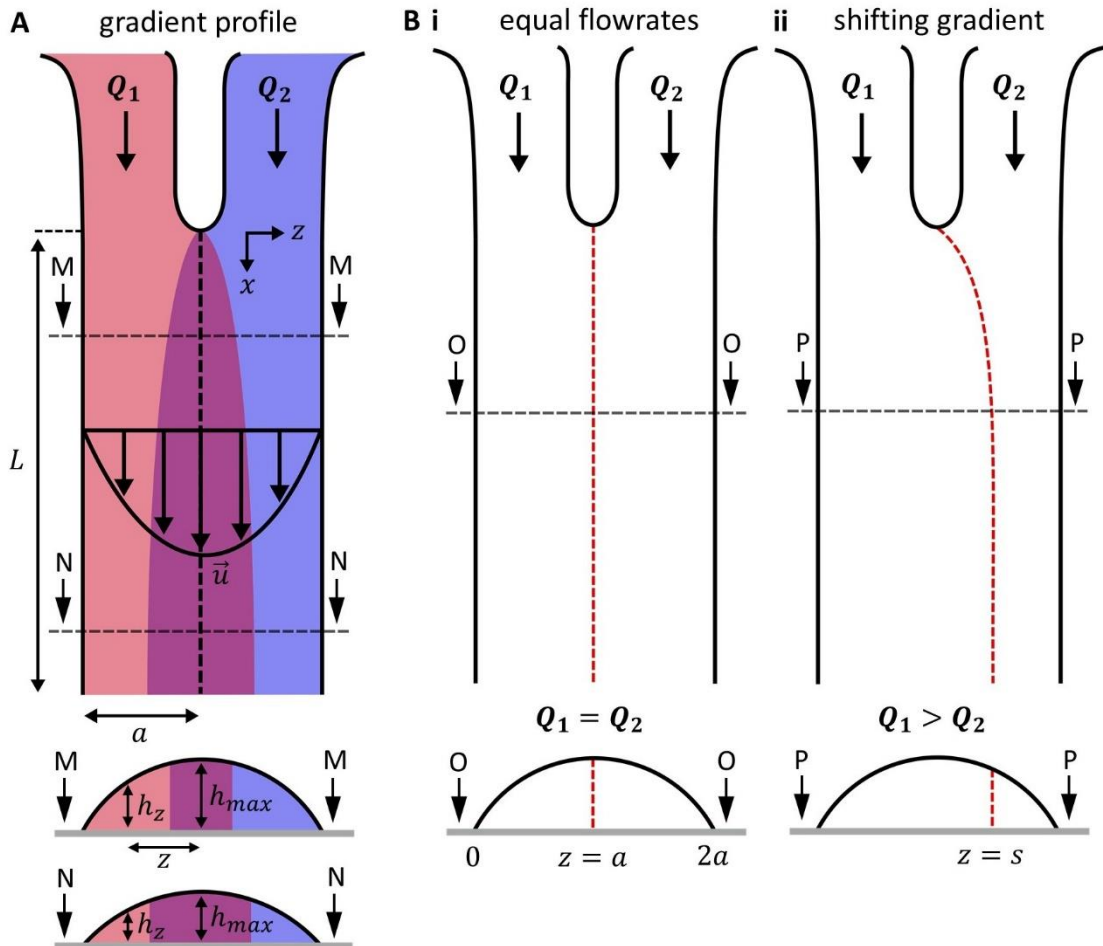


Figure S5. Characterizing stable and shifting gradients in active circuits. (A) General gradient and conduit characteristics. Illustration of a conduit with input streams Q_1 (red) and Q_2 (blue). Streams meet in the middle of the conduit below the junction, and diffusion creates a steady gradient across the width

(purple area). Gradient width increases in the x -direction (as shown in cross-sections M-M and N-N). L = conduit length, a = conduit half width, \vec{u} = velocity field, h_{max} = max conduit height, h_z = conduit height at z . **(B)** Location of gradient centerline for various input-stream flow-rate ratios. Plans are shown above, and cross-section profiles at O-O and P-P below. **(i)** For equal flow rates (i.e., $Q_1 = Q_2$), streams meet in the middle of the conduit at location $z = a$ (denoted by the red dashed line). **(ii)** When the flow rate is increased in one arm relative to the other (i.e., $Q_1 > Q_2$), this centreline shifts in the direction of the weaker stream to location $z = s$.

To validate our assumptions for predicting gradients in the case where input flow rates are equal (**Figure S5Bi**), we compare predictions using the average velocity along the conduit centerline (**Figure S6i**) to predictions made using a numerical approach. This approach mirrors the case for the shifted gradient described for **Figure S5Bii**, except that we first begin by predicting t using the mean velocity at the conduit centerline, and progressively shift the mean velocity used to calculate t to a distance $a/2$ from the centreline (**Figure S6ii**).

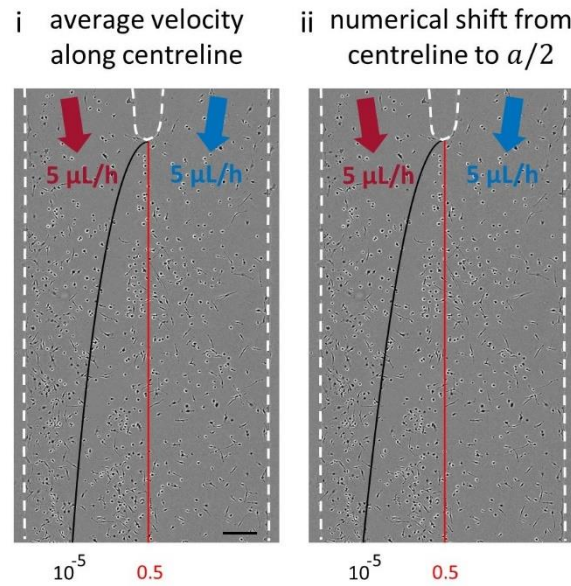


Figure S6. Comparing gradient prediction methods in active circuits. Images of central conduit in circuit like that shown in Figure 5 at $t = 24$ h, with input flow rate $Q = 10 \mu\text{L/h}$. Scale bar = $250 \mu\text{m}$. **(i)** Two contours at each end of the gradient predicted using the average velocity along the conduit centerline. **(ii)** Similar contours predicted using a numerical approach in which the average velocity is first taken along the centerline and then progressively shifted by a distance $a/2$.

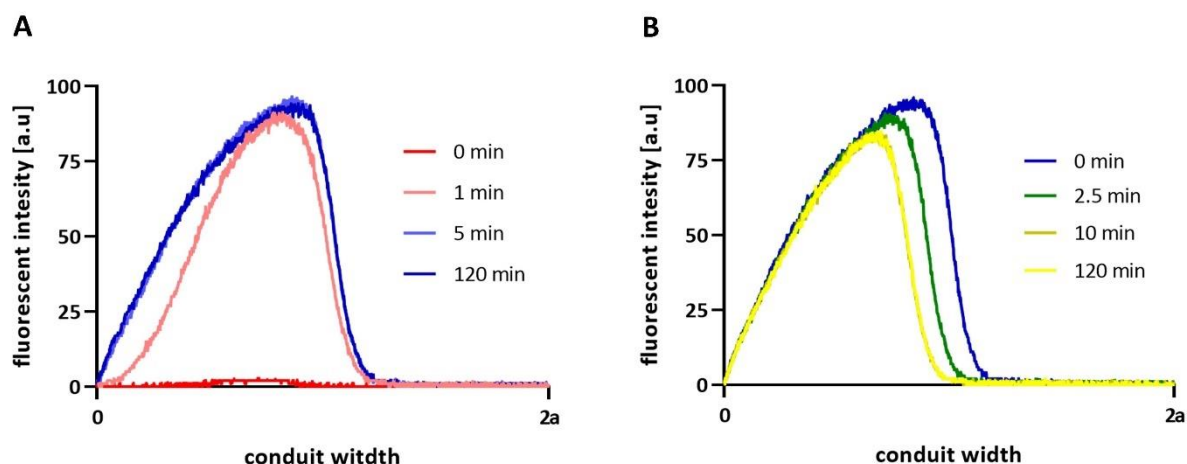


Figure S7. Tracking gradient formation, stability, and shift. A gradient of fluorescein is established in an ‘m’-shaped conduit. Fluorescence intensity (arbitrary unit) is then measured and monitored 1.5 mm downstream from the junction as the gradient is first established, becomes stable, and later shifted. **(A)** Fluorescein is infused through one arm at 5 $\mu\text{L/h}$ and PBS through the other arm at 5 $\mu\text{L/h}$. A movie of the gradient establishing in the conduit is taken, and the fluorescence intensity across the width of the conduit is measured (from 0 to 2a, a = conduit half width). The fluorescence profile is plotted at $t = 0$ (the pumps start to infuse PBS and fluorescein) and 1, 5, and 120 min later. The graph demonstrates that the gradient is established and fully developed after 5 min and remains stable over 2 h (see Movie S18). **(B)** The same gradient is now shifted towards the side of the conduit containing fluorescein by increasing the flowrate of PBS to 7.15 $\mu\text{L/h}$ and decreasing the flowrate of fluorescein to 2.85 $\mu\text{L/h}$ (as in Figure 5B). Fluorescence intensity is again recorded and shows that the gradient remains stable in the new location over 2 h (see Movie S19).

Assessing the effect of circuit geometry on cell velocity

Fluid-walled conduits have cross-sections that sections of a circle, and conduit height decreases from the centerline to the wall (**Figure S5**). Consequently, cells growing in such conduits have varying volumes of medium above them depending on their location in the conduit. We thus investigate the effect of cell position on cell behavior using passive dumbbell-shaped circuits filled with cells, to assess whether these changing heights bias cell behavior. We expose cells in the circuits to either plain cell culture medium or uniform distributions of 10 nM C5a (no gradient) and image them over 48 h. We then segment circuits into 19 distinct regions and compare cell velocities in each (**Figure S8**). In this way, we show that average cell velocities throughout circuits are nearly identical and thus that changing heights do not impact cell behavior.

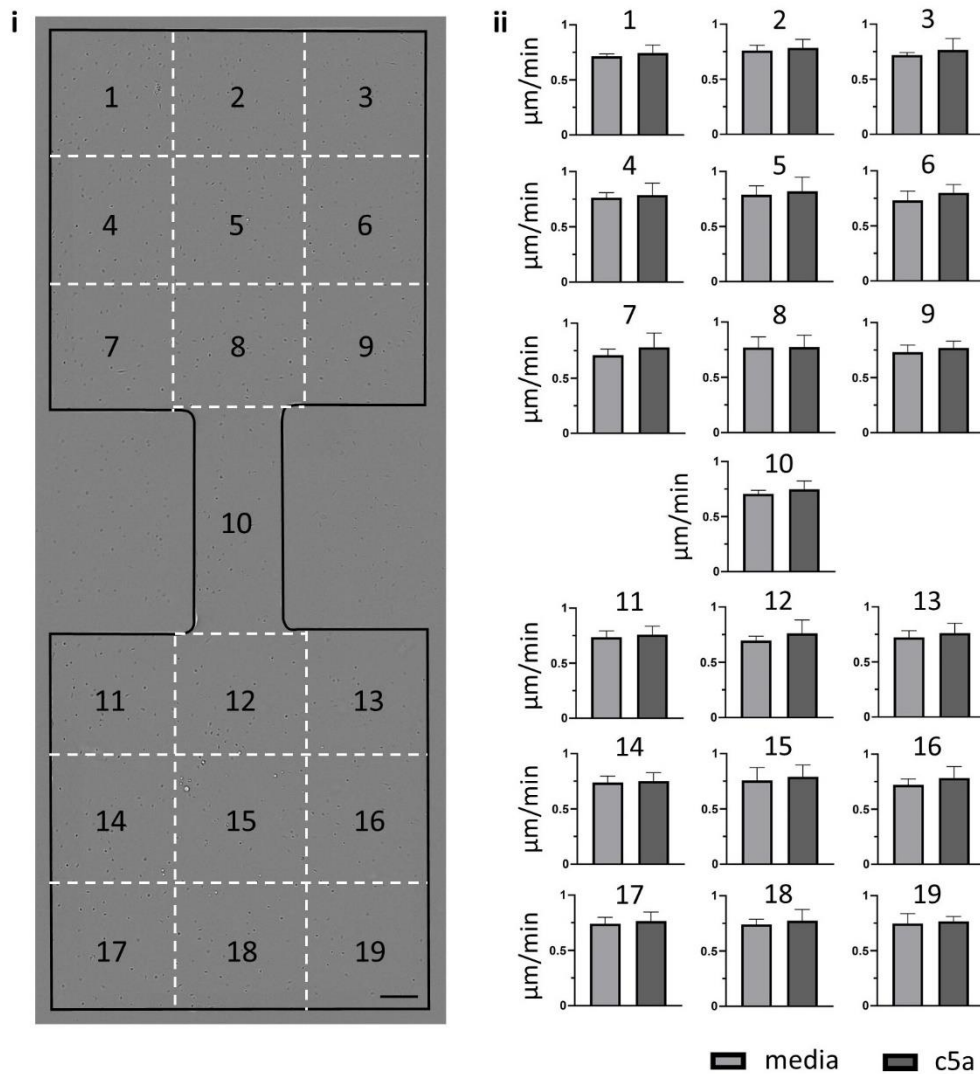


Figure S8. Location within a circuit has no effect on velocity of BMDM movement. Control experiments in which cells are present throughout the entire circuit are performed to identify potential biases in cell behavior at various circuit locations. Average cell velocities are analyzed in circuits containing only medium or uniform distributions of 10 nM C5a (without gradient; 3 biological replicates for each condition). Circuits like those in Figure 2 are imaged over 48 h and cell trajectories analyzed. Circuits are segmented into 19 regions and average cell velocities are presented for each region. **(i)** Image of a circuit plus cells, with superimposed plan showing the 19 regions. Scale bar: 250 μm . **(ii)** Cell velocities for both conditions and all regions (+ SD). Average cell velocities are unaffected by circuit location or the presence of C5a.

Movies

Movie S1. Macrophages in the top chamber of a dumbbell circuit chemotaxing in a 10 nM gradient of C5a (as in Figure 2). Cells are initially contained within the top chamber (not visible), and few can be seen at the top of the conduit (length = 1.5 mm). Cells chemotax through the conduit over 48 h towards the C5a chamber at the bottom.

Movie S2. Macrophages in the conduit of a dumbbell circuit chemotaxing in a 10 nM gradient of C5a (as in Figure 2). Cells are initially uniformly distributed in the conduit (length = 1.5 mm). Most cells in the bottom half of the conduit chemotax over 48 h towards the C5a chamber (bottom). However, most cells in the top half do not chemotax and are chemokinetic.

Movie S3. Macrophages in the conduit of a dumbbell circuit with medium everywhere (as in Figure 2 except no C5a is present). Cells are initially uniformly distributed in the conduit (length = 1.5 mm). In the absence of a gradient, cells are chemokinetic and move randomly over 48 h.

Movie S4. Macrophages in the conduit of a dumbbell circuit with uniform distribution of 10 nM C5a (as in Figure 2 except C5a is everywhere). Cells are uniformly distributed in the conduit (1.5 mm). In the absence of a C5a gradient (uniform distribution of C5a), the cells are chemokinetic and move randomly over 48 h.

Movie S5. Macrophages in 6 mm conduit chemotaxing in a 10 nM gradient of C5a (as in Figure 3). Cells are initially uniformly distributed in the conduit (length = 6 mm). Only cells initially at the bottom of the conduit chemotax over 48 h towards the C5a chamber; cells initially located behind this band of responding cells do not chemotax and are chemokinetic.

Movie S6. Macrophages in top third of a 6 mm conduit chemotaxing in a 10 nM gradient of C5a (as in Figure 3). Cells are initially distributed in the top third of the conduit (length = 6 mm). Seven cells at the front closest to C5a chemotax over 48 h towards the attractant; cells behind these ones do not chemotax and are chemokinetic.

Movie S7. Macrophages in middle third of a 6 mm conduit chemotaxing in a 10 nM gradient of C5a (as in Figure 3). Cells are initially distributed in the middle third of the conduit (length = 6 mm). Only cells at the front chemotax over 48 h towards the C5a chamber; cells behind these ones do not chemotax and are chemokinetic.

Movie S8. Macrophages in bottom third of a 6 mm conduit chemotaxing in a 10 nM gradient of C5a (as in Figure 3). Cells are initially distributed in the bottom third of the conduit (length = 6 mm). Only

cells at the front chemotax over 48 h towards the C5a chamber; cells behind these ones do not chemotax and are chemokinetic.

Movie S9. C5a-receptor KO macrophages in the top conduit of a 3-well dumbbell circuit in a 10 nM gradient of C5a (as in Figure 3). C5a-receptor KO cells are uniformly distributed in the top conduit (length = 1.5 mm) of a 3-well dumbbell circuit. In the presence of a C5a gradient, cells are chemokinetic and move randomly over 48 h.

Movie S10. WT macrophages in the bottom conduit of a 3-well dumbbell circuit in a 10 nM gradient of C5a (as in Figure 4). WT cells are uniformly distributed in the bottom conduit (1.5 mm) of a 3-well dumbbell circuit. In the presence of a C5a gradient, most cells in the top half of the conduit chemotax over 48 h towards the C5a chamber, which some are seen entering (top). However, most cells in the bottom half do not chemotax and are chemokinetic.

Movie S11. Macrophages in ‘m’-shaped circuit under a steady gradient of 10 nM C5a (as in Figure 5). Cells plated in the central conduit of an ‘m’-shaped circuit are exposed to a steady gradient of C5a over 48 h. Medium is perfused through the left arm (5 $\mu\text{L/h}$) and C5a through the right (5 $\mu\text{L/h}$). A gradient is established across the center of the conduit, and cells chemotax from into this region from the left, leaving behind a cell-deplete zone.

Movie S12. Macrophages in ‘m’-shaped circuit under a gradient of 10 nM C5a shifted abruptly to the right (as in Figure 5). Cells plated in the central conduit of an ‘m’-shaped circuit are exposed to a steady gradient of C5a over 24 h; medium is perfused through the left arm (5 $\mu\text{L/h}$) and C5a through the right (5 $\mu\text{L/h}$). Cells on the left chemotax into the center of the conduit to leave behind a cell-deplete zone. After 24 h, the gradient is shifted abruptly 200 μm to the right by increasing medium flow (7.15 $\mu\text{L/h}$) and decreasing C5a flow (2.85 $\mu\text{L/h}$), and then flow is kept steady for an additional 24 h. Cells in the center of the conduit respond by chemotaxing further to the right.

Movie S13. Macrophages in ‘m’-shaped circuit under a gradient of 10 nM C5a shifting continuously to the right (as in Figure 5). Cells plated in the conduit of an ‘m’-shaped circuit are exposed to a steady gradient of C5a over 24 h. Medium is perfused through the left arm (5 $\mu\text{L/h}$) and C5a through the right (5 $\mu\text{L/h}$). Cells on the left chemotax into the center of the conduit to leave behind a cell-deplete zone. After 24 h, the gradient is shifted continuously over the next 24 h by 750 μm to the right, by gradually increasing medium flow (from 5 to 9.98 $\mu\text{L/h}$) and decreasing C5a flow (from 5 to 0.02 $\mu\text{L/h}$). During this time, cells chemotax but not as strongly as previously. At the end of the continuous shift, the gradient is kept steady in the new location (150 μm from the right wall) for an additional 24 h. A new band of cells then responds by chemotaxing strongly into this region, creating a cell-deplete zone in the right half of the conduit.

Movie S14. Summary of movies S1-S4. Side-by-side view of movies S1-S4 to compare the cell responses of each setup.

Movie S15. Summary of movies S5-S8. Side-by-side view of movies S5-S8 to compare the cell responses of each setup.

Movie S16. Summary of movies S9-S10. Side-by-side view of movies S9-S10 to compare the cell responses of each setup.

Movie S17. Summary of movies S11-S13. Side-by-side view of movies S11-S13 to compare the cell responses of each setup.

Movie S18. Establishing a stable fluorescein gradient in an ‘m’-shaped conduit. Fluorescein is infused through one arm of the conduit (top) at 5 $\mu\text{L/h}$ and PBS through the other arm (bottom) at 5 $\mu\text{L/h}$. Dashed white lines show the conduit pinning lines. After 5 min, the concentration gradient of fluorescein is fully developed and stable across the conduit centerline (see Figure S7), and the conduit is imaged over 1 h just below the junction.

Movie S19. Shifting a fluorescein gradient in an ‘m’-shaped conduit. The stable fluorescein gradient of Movie S18 is now shifted 200 μm from the centerline towards the top side of the conduit (fluorescein side) by increasing the flowrate of PBS to 7.15 $\mu\text{L/h}$ and decreasing the flowrate of fluorescein to 2.85 $\mu\text{L/h}$ (as in Figure 5B). The gradient is then seen rapidly shifting to its new location to become stable after ~ 6 min, and the conduit is imaged for a further 30 min.